TKK Dissertations 143
Espoo 2008

MODAL ANALYSIS OF LAYER-STRUCTURED OPTICAL FIBERS

Doctoral Dissertation

Markus Hautakorpi

Helsinki University of Technology
Faculty of Information and Natural Sciences
Department of Applied Physics

TKK Dissertations 143
Espoo 2008

MODAL ANALYSIS OF LAYER-STRUCTURED OPTICAL FIBERS

Doctoral Dissertation

Markus Hautakorpi

Dissertation for the degree of Doctor of Science in Technology to be presented with due permission of the Faculty of Information and Natural Sciences for public examination and debate in Auditorium AS1 at Helsinki University of Technology (Espoo, Finland) on the 1st of December, 2008, at 12 noon.

Helsinki University of Technology
Faculty of Information and Natural Sciences
Department of Applied Physics

Teknillinen korkeakoulu
Informaatio- ja luonnontieteiden tiedekunta
Teknillisen fysiikan laitos

Distribution:
Helsinki University of Technology
Faculty of Information and Natural Sciences
Department of Applied Physics
P.O. Box 3500
FI - 02015 TKK
FINLAND
URL: http://tfy.tkk.fi/
Tel. +358-9-451 3153
Fax +358-9-451 3155
E-mail: markus.hautakorpi@tkk.fi

ISBN 978-951-22-9631-6
ISBN 978-951-22-9632-3 (PDF)
ISSN 1795-2239
ISSN 1795-4584 (PDF)
URL: http://lib.tkk.fi/Diss/2008/isbn9789512296323/

TKK-DISS-2527

Multiprint Oy
Espoo 2008

ABSTRACT OF DOCTORAL DISSERTATION	HELSINKI UNIVERSITY OF TECHNOLOGY P. O. BOX 1000, FI-02015 TKK http://www.tkk.fi

Author Markus Hautakorpi

Name of the dissertation

Modal analysis of layer-structured optical fibers

Manuscript submitted 19.08.2008	Manuscript revised
Date of the defence 01.12.2008	
☐ Monograph	☒ Article dissertation (summary + original articles)
Faculty	Faculty of Information and Natural Sciences
Department	Department of Applied Physics
Field of research	Optics
Opponent(s)	Professor Jürgen Jahns
Supervisor	Professor Matti Kaivola
Instructor	Professor Matti Kaivola, Docent Hanne Ludvigsen

Abstract

Numerical modeling techniques play a key role in the development of new fiber optics, e.g., for telecommunications or sensing applications. In particular, the refractive-index profiles of various specialty optical fibers are increasingly designed with numerical tools. In this thesis, analytical and numerical mode-analysis techniques are applied to layer-structured specialty fibers as well as to partially coherent optical fields. The work is divided into three parts.

In the first part, hollow-core and annular-core optical fibers are considered. The accuracy of the weak-guidance approximation for the low-order modes of such fibers is first assessed. Then, the approximation is employed to investigate the use of hollow-core multimode fibers in evanescent-wave guiding of laser-cooled atoms. Two schemes for creating the required evanescent-wave field on the inner surface of the fiber are analyzed. These are based on the selective excitation of tubular fiber modes with Laguerre–Gaussian input beams and on the dithering of a Gaussian beam at the fiber input to average out the speckles due to multimode interference. The first part of the thesis is concluded with a full-vector analysis of the self-imaging properties of annular-core fibers.

In the second part, microstructured optical fibers with coated inclusions are studied. The effect of high-refractive-index dielectric inclusions on the photonic bandgap of a photonic-crystal fiber is characterized. Also, a novel design for a fiber-integrated surface-plasmon-resonance sensor based on a three-hole microstructured fiber with metal inclusions is proposed. The sensor makes use of an aqueous analyte infiltrated into the fiber pores.

In the third part, the coherent-mode analysis of partially coherent light is applied to a random, stationary optical field which rotates with respect to an observer. The spectral changes due to the rotation are exemplified for a field with Gaussian Schell-model space correlations.

Keywords modal analysis, hollow optical fiber, self-imaging, fiber-optical sensor, optical coherence	
ISBN (printed) 978-951-22-9631-6	ISSN (printed) 1795-2239
ISBN (pdf) 978-951-22-9632-3	ISSN (pdf) 1795-4584
Language English	Number of pages 47 p. + app. 31 p.
Publisher Helsinki University of Technology, Department of Applied Physics	
Print distribution Helsinki University of Technology, Department of Applied Physics	
☒ The dissertation can be read at http://lib.tkk.fi/Diss/2008/isbn9789512296323/	

VÄITÖSKIRJAN TIIVISTELMÄ	TEKNILLINEN KORKEAKOULU PL 1000, 02015 TKK http://www.tkk.fi

Tekijä Markus Hautakorpi

Väitöskirjan nimi

Kerrosrakenteisten valokuitujen optinen kenttämuotoanalyysi

Käsikirjoituksen päivämäärä 19.08.2008	Korjatun käsikirjoituksen päivämäärä
Väitöstilaisuuden ajankohta 01.12.2008	
☐ Monografia	☒ Yhdistelmäväitöskirja (yhteenveto + erillisartikkelit)

Tiedekunta	Informaatio- ja luonnontieteiden tiedekunta
Laitos	Teknillisen fysiikan laitos
Tutkimusala	optiikka
Vastaväittäjä(t)	professori Jürgen Jahns
Työn valvoja	professori Matti Kaivola
Työn ohjaaja	professori Matti Kaivola, dosentti Hanne Ludvigsen

Tiivistelmä

Laskennallisilla menetelmillä on keskeinen rooli, kun uutta kuituoptiikkaa kehitetään esimerkiksi tietoliikenne- tai sensorisovellusten tarpeisiin. Varsinkin uusia valokuituja suunniteltaessa taitekerroinprofiili räätälöidään yhä useammin laskennallisilla työkaluilla. Tässä väitöskirjassa laskennallista ja analyyttistä kenttämuotoanalyysiä sovelletaan kerrosrakenteisten valokuitujen sekä osittain koherenttien optisten kenttien tutkimiseen. Työ jakautuu kolmeen osaan.

Ensimmäisessä osassa tarkastellaan valokuituja, joiden ydin on poikkileikkaukseltaan rengasmainen. Ensin määritetään optisen skalaariteorian (weak-guidance approximation) soveltuvuus tällaisten valokuitujen alimpien kenttämuotojen analysointiin. Skalaariteoriaa hyödyntäen seuraavaksi tutkitaan onttojen monimuotokuitujen käyttöä laserjäähdytettyjen atomien kuljettamiseen. Tähän tarvittava putkimainen, vaimeneva optinen kenttä voidaan tuottaa joko kytkemällä kuituun Laguerre–Gaussinen säde tai moduloimalla tavallisen Gaussisen säteen sisääntulokulmaa kuidun päässä muotokohinan tasoittamiseksi. Työn ensimmäisen osan lopussa kartoitetaan rengasytimisten valokuitujen käytettävyyttä optisen kentän itseiskuvautumisessa (self-imaging).

Toisessa osassa tarkastellaan mikrorakenteisia valokuituja, joiden sisäpinnoille on kasvatettu tasainen materiaalikerros. Aluksi karakterisoidaan korkean taitekertoimen eristemateriaalin vaikutus onton fotonikidekuidun transmissiokaistaan. Lisäksi ehdotetaan uutta rakennetta kuituun integroitavan, pintaplasmonien resonanssiominaisuuksia hyödyntävän sensorin toteuttamiseen. Ehdotus pohjautuu kolmireikäiseen mikrorakennekuituun, jossa ilmahuokoset on ensin päällystetty metallilla ja tämän jälkeen täytetty vesipohjaisella analyytillä.

Kolmannessa osassa sovelletaan osittain koherentin valon koherenttimuotokehitelmää satunnaisesti värähtelevään, stationääriseen valokenttään, joka on pyörivässä liikkeessä havaitsijan suhteen. Pyörimisestä johtuvia spektrimuutoksia havainnollistetaan olettamalla kentän paikkakorrelaatiot Gaussisen Schell-mallin mukaisiksi.

Asiasanat kenttämuotoanalyysi, ontto valokuitu, itseiskuvautuminen, valokuitusensori, optinen koherenssi

ISBN (painettu) 978-951-22-9631-6	ISSN (painettu) 1795-2239
ISBN (pdf) 978-951-22-9632-3	ISSN (pdf) 1795-4584
Kieli englanti	Sivumäärä 47 s. + liit. 31 s.

Julkaisija Teknillinen korkeakoulu, Teknillisen fysiikan laitos

Painetun väitöskirjan jakelu Teknillinen korkeakoulu, Teknillisen fysiikan laitos

☒ Luettavissa verkossa osoitteessa http://lib.tkk.fi/Diss/2008/isbn9789512296323/

Preface

The research work summarized in this thesis has been carried out in the Optics and Molecular Materials (OMM) Laboratory and in the Micro and Nanosciences (MNT) Laboratory of Helsinki University of Technology.

I am indebted to Professor Matti Kaivola and Docent Hanne Ludvigsen for the opportunity to work in their research groups and for the guidance I have received on the way. Occasional guidance during my years at OMM were also given by Docents Andriy Shevchenko and Tero Setälä, which is deeply appreciated. Many other fellow workers in OMM and MNT have as well furthered the completion of this work: my compliments go to Jari Lindberg, Maija Mattinen, Klas Lindfors, Antti Jaakkola, Miika Heiliö, Antti Hakola, Arri Priimägi, Esa Räikkönen, Hannu Hoffrén, Ossi Kimmelma, Timo Hakkarainen, and Orvokki Nyberg. I am grateful to Dr. Robert B. Vincelette Jr. for his useful remarks on the usage of American English. I also want to thank the IT Center for Science (CSC) for providing computational resources where necessary.

Enjoyable counterbalance to my work has been provided by my friends, of whom I especially wish to thank Hannu & Hanna Risku, Tuomo Ylinen, Santtu Lehtiniemi, Timo & Maija Kontro with their offsprings, Pekka Manninen, Matti Peltonen, Oke Rouhe, and Niina Numminen.

The financial support by the Academy of Finland, the Jenny and Antti Wihuri Foundation, the Finnish Foundation for Technology Promotion, the Finnish Cultural Foundation, and the Alfred Kordelin Foundation is gratefully acknowledged.

Finally, I heartily thank my parents Esko and Sisko, my brother Esa, and my sister Sari for their continuous support and encouragement. I likewise wish to thank my wife Kaisa for her love and patience during these years.

Espoo, August 2008

Markus Hautakorpi

List of publications

This thesis is a review of the author's work on modal analysis of optical fibers and partially coherent optical fields. It consists of an overview and the following selection of the author's publications in peer-reviewed journals:

I. M. Hautakorpi and M. Kaivola, "Modal analysis of M-type-dielectric-profile optical fibers in the weakly guiding approximation," J. Opt. Soc. Am. A **22,** 1163–1169 (2005).

II. M. Hautakorpi, A. Shevchenko, and M. Kaivola, "Spatially smooth evanescent-wave profiles in a multimode hollow optical fiber for atom guiding," Opt. Commun. **237,** 103–110 (2004).

III. M. Hautakorpi and M. Kaivola, "Modal analysis of the self-imaging phenomenon in optical fibers with an annular core," Appl. Opt. **45,** 6388–6392 (2006).

IV. M. Hautakorpi, M. Mattinen, and H. Ludvigsen, "Surface-plasmon-resonance sensor based on three-hole microstructured optical fiber," Opt. Express **16,** 8427–8432 (2008).

V. M. Hautakorpi, J. Lindberg, T. Setälä, and M. Kaivola, "Rotational frequency shifts in partially coherent optical fields," J. Opt. Soc. Am. A **23,** 1159–1163 (2006).

Throughout the overview, these papers are referred to by their Roman numerals.

Author's contribution

The research reviewed in this thesis has been carried out in the Optics and Molecular Materials Laboratory (during the years 2003–2006) and in the Micro and Nanosciences Laboratory (during the years 2006–2008) of Helsinki University of Technology.

The author has been at the center of the research work reported in Papers I–V. He has created Paper I in its entirety. For Paper II, he has implemented the numerical methods and performed the analyses. Paper III has been fully created by the author. The sensor construction reported in Paper IV was devised and numerically characterized by the author. The author has instigated and carried out the research of Paper V. He has prepared the manuscripts for all of these papers.

Other peer-reviewed publications by the author or to which the author has contributed:

- A. Shevchenko, P. Ryytty, T. Kajava, M. Hautakorpi, and M. Kaivola, "Single-longitudinal-mode selection in a nanosecond-pulsed dye laser," Appl. Phys. B **74,** 349–354 (2002).
- A. Jaakkola, A. Shevchenko, K. Lindfors, M. Hautakorpi, E. Il'yashenko, T. H. Johansen, and M. Kaivola, "Reconfigurable atom chip on a transparent ferrite-garnet film," Eur. Phys. J. D **35,** 81–85 (2005).
- M. Hautakorpi, H. Hoffrén, J. Tiilikainen, and H. Ludvigsen, "Photonic bandgaps in photonic crystal fibers with coated high-index inclusions," in Conference on Lasers and Electro-Optics (CLEO/QELS 07), Baltimore, Maryland, US, May 6–11 2007, paper JTuA65.
- M. Hautakorpi, M. Mattinen, and H. Ludvigsen, "Surface-plasmon-resonance sensor based on suspended-core microstructured optical fiber," in OECC/ ACOFT 2008, Sydney, Australia, July 7–10 2008, paper WeE–2.
- M. Hautakorpi, M. Mattinen, and H. Ludvigsen, "Novel sensor concept based on microstructured optical fiber with metal inclusions," in European Conference on Optical Communication (ECOC 2008), in Brussels, Belgium, September 21–25 2008, paper We3B6.

Abbreviations

ACF	Annular-core (optical) fiber
FEM	Finite-element method
HOF	Hollow(-core) optical fiber
LG	Laguerre–Gaussian
LP	Linearly polarized
MOF	Microstructured optical fiber
PBF	Photonic-bandgap fiber
PML	Perfectly matched layer
TE	Transverse electric
TM	Transverse magnetic
WGA	Weak-guidance approximation (Weakly guiding approximation)

Contents

Chapter 1

Introduction

Kilometer-wise, the most common type of optical fiber today is the step-index, single-mode fiber which forms the backbone of the global telecommunications network. In addition, various specialty optical fibers are employed, e.g., for dispersion and polarization controlling, amplification, and filtering [1]. Specialty fibers are widely used also in other fields of technology and science such as nonlinear optics [2, 3], (medical) imaging [4], and especially sensing applications [5–7]. For the special purposes in particular, various microstructures can be employed to gain substantial design flexibility. Indeed, microstructured optical fibers have enabled the guiding of light along an air channel with low loss by means of the photonic-bandgap or the low-density-of-states effect [8], and the generation of supercontinuum radiation covering the near-infrared and visible spectral bands [9]. The applications of these and other fiber-optical components and devices continue to grow rapidly in number.

The design of novel specialty and microstructured optical fibers often relies on numerical modeling, as the structures can be very complex and ample computational resources are readily available. A powerful approach for the modeling task is that of modal analysis where the propagation-invariant field forms of the waveguide are identified. Their generic mathematical properties can then be employed to find out, for instance, the excitation efficiency of a particular fiber mode, multimode interference patterns, and the characteristics of spatial transitions in terms of local modes. Yet, analytic and semi-analytic approaches remain at least equally important in that they provide insight into the problem at hand and help reduce the computation times. The same holds true for approximative techniques, if these are chosen wisely enough. In this thesis, a host of mode-analysis techniques are applied to specialty and microstructured optical fibers as well as to partially coherent free-space fields. The work is divided into three parts each of which is briefly described in the following.

In the first part of the thesis, the modal fields of hollow-core optical fibers (HOFs) and annular-core optical fibers (ACFs) are considered. In a HOF the section surrounding the optical axis is empty, whereas in an ACF this section is similar to the cladding outside the core. Although there are no ubiquitous "killer" applications for these fibers, they have found use in many contexts. For instance, besides the applications considered in this thesis, HOFs can serve as modal filters or mode converters [10] and the output beam of an ACF as an optical trap for micron-size particles [11]. Quite commonly, the modal analysis of HOFs and ACFs is performed in terms of scalar fields by adopting the weak-guidance approximation (WGA) [12]. The legitimacy of using this approach to describe the low-order modal fields in HOFs and ACFs is established in Sec. 3.1 [Paper I]. One of the most exciting applications of HOFs is in the field of atom optics where they can act as conveyor tubes for slow, laser-cooled atoms [13]. A prerequisite for this function is a spatially smooth field that is strongly localized in the vicinity of the inner wall of a HOF. Weakly guided fiber modes are employed in Sec. 3.2 to analyze two methods for creating such a smooth atom-guiding field onto the HOF wall [Paper II]. Thin-core ACFs, on the other hand, can be used to produce self-images, or Talbot images, of annular wavefields [14–16]. This has proven to be useful, e.g., in phase-locking of a circular array of fiber lasers [17, 18]. The rationale behind the self-imaging capability builds on the scalar-field approximation which, as demonstrated in Sec. 3.1, can be particularly unreliable in the case of a thin-core ACF. The results of a full-vector investigation of the self-imaging phenomenon are presented in Sec. 3.3 [Paper III].

In the second part, the electromagnetic fields of holey, microstructured optical fibers with coated dielectric and metal inclusions are considered. The motivation for modeling such structures arises mainly from a recent experimental demonstration where high-pressure chemical deposition techniques were successfully used to uniformly coat the surfaces of the minuscule fiber holes with semiconductors and metals [19]. Advancements of this kind pave the way, e.g., for compact, fiber-integrated optoelectronic device concepts. To support the experimental efforts, the effect of a uniform, high-index dielectric coating on the transmission characteristics of an off-the-shelf photonic-bandgap fiber is specified in Sec. 4.1. Accordingly, the spectral position of the photonic bandgap will signal the thickness of the coating. Furthermore, in Sec. 4.2, a novel fiber-integrated sensor concept for aqueous analytes is put forward [Paper IV]. The sensor design is based on the excitation of surface-plasmon-polariton resonances in a three-hole microstructured optical fiber with metal-coated pore surfaces.

In the third and final part comprising Ch. 5, the mode-analysis tools are applied to partially coherent, free-space optical fields. In the case of a completely coherent field, the optical angular-momentum content is known to be responsible for the spectral shifts that occur when the field rotates with respect to an observer [20].

Such shifts manifest themselves in the direction of the rotation axis and are thus different from the ordinary, linear Doppler shifts. By expanding a partially coherent field in terms of angular-momentum-carrying modes, it is shown that the coherence properties of the field will significantly affect the quality of the rotational shifts [Paper V].

Chapter 2

Modal analysis of electromagnetic fields

In this chapter, the principles of mode-analysis techniques are covered. Starting from Maxwell's equations, the relevant characteristics of the modal solutions of the wave equation in fiber waveguides and in free space are presented. A special class of free-space beams possessing orbital angular momentum is considered. Finally, the coherent-mode representation of partially coherent beams is briefly surveyed.

2.1 Modal fields in optical fibers

2.1.1 Wave equations

The electromagnetic fields in optical fiber waveguides are governed by the macroscopic Maxwell's equations which in their complete form read as [21, 22]

$$\nabla \cdot \mathbf{D}(\mathbf{r},t) = \rho_f(\mathbf{r},t), \tag{2.1}$$

$$\nabla \cdot \mathbf{B}(\mathbf{r},t) = 0, \tag{2.2}$$

$$\nabla \times \mathbf{E}(\mathbf{r},t) = -\frac{\partial \mathbf{B}(\mathbf{r},t)}{\partial t}, \tag{2.3}$$

$$\nabla \times \mathbf{H}(\mathbf{r},t) = \mathbf{J}(\mathbf{r},t) + \frac{\partial \mathbf{D}(\mathbf{r},t)}{\partial t}. \tag{2.4}$$

Here, $\mathbf{E}$ and $\mathbf{H}$ are the electric and magnetic fields, respectively, and $\mathbf{D}$ and $\mathbf{B}$ denote the electric and magnetic flux densities, respectively. Furthermore, the term $\mathbf{J}$ is the current density, ρ_f is the charge density, $\mathbf{r}$ is the spatial coordinate, and

t denotes time. Time-harmonic solutions describing strictly monochromatic fields can be sought for by writing [23]

$$\mathbf{E}(\mathbf{r},t) = \mathbf{E}(\mathbf{r},\omega)\exp(i\omega t), \quad (2.5)$$
$$\mathbf{H}(\mathbf{r},t) = \mathbf{H}(\mathbf{r},\omega)\exp(i\omega t), \quad (2.6)$$

where ω is the angular frequency of light. In this representation, the real parts of the expressions correspond to the physical fields [1]. By assuming a linear, isotropic, and nonmagnetic medium, one can write the constitutive relations as [24]

$$\mathbf{D}(\mathbf{r},\omega) = \epsilon_0\epsilon_r(\mathbf{r},\omega)\mathbf{E}(\mathbf{r},\omega), \quad (2.7)$$
$$\mathbf{B}(\mathbf{r},\omega) = \mu_0\mathbf{H}(\mathbf{r},\omega), \quad (2.8)$$

where ϵ_0 and μ_0 are the permittivity and permeability of free space, respectively, and ϵ_r denotes the relative, material-dependent permittivity. To study the modal fields in fibers with metallic (lossy) inclusions, ohmic conduction currents can be included by writing

$$\mathbf{J}(\mathbf{r},\omega) = \sigma(\mathbf{r},\omega)\mathbf{E}(\mathbf{r},\omega) \quad (2.9)$$

where σ is the conductivity [24].

By taking the curl of Eq. (2.3), and by using Eqs. (2.4)–(2.9), one obtains the wave equation for the electric field

$$\nabla\times\nabla\times\mathbf{E}(\mathbf{r},\omega) - \frac{\omega^2}{c^2}\left[\epsilon_r(\mathbf{r},\omega) - \frac{i\sigma(\mathbf{r},\omega)}{\omega\epsilon_0}\right]\mathbf{E}(\mathbf{r},\omega) = 0 \quad (2.10)$$

where $c = 1/\sqrt{\epsilon_0\mu_0}$ denotes the speed of light in free space. The term in the square brackets can be identified with the complex, relative dielectric function which, from this point on, is also represented by the variable ϵ_r [24]. Similarly, by starting from Eq. (2.4), one can derive the wave equation for the magnetic field in the form

$$\nabla\times\frac{1}{\epsilon_r(\mathbf{r},\omega)}\nabla\times\mathbf{H}(\mathbf{r},\omega) - k_0^2\mathbf{H}(\mathbf{r},\omega) = 0 \quad (2.11)$$

where the wavenumber is denoted by $k_0 = \omega/c$. For homogeneous media, the wave equations simplify to

$$\nabla^2\mathbf{E}(\mathbf{r},\omega) + k_0^2 n^2(\omega)\mathbf{E}(\mathbf{r},\omega) = 0, \quad (2.12)$$
$$\nabla^2\mathbf{H}(\mathbf{r},\omega) + k_0^2 n^2(\omega)\mathbf{H}(\mathbf{r},\omega) = 0, \quad (2.13)$$

where the refractive index is introduced through the relation $n^2 = \epsilon_r$ [25].

To obtain the modes of an optical fiber, the z-dependence along the fiber is separated by writing

$$\mathbf{E}_j(\mathbf{r},\omega) = \mathbf{E}_j(\mathbf{r}_\perp,\omega)\exp[-i\beta_j(\omega)z], \quad (2.14)$$
$$\mathbf{H}_j(\mathbf{r},\omega) = \mathbf{H}_j(\mathbf{r}_\perp,\omega)\exp[-i\beta_j(\omega)z], \quad (2.15)$$

where β_j is the propagation constant of the jth mode and $\mathbf{r}_\perp$ describes a position vector in the transverse plane of the fiber. In principle, the wave equations hold an infinite number of transverse modes in the form of Eqs. (2.14) and (2.15) for a given optical frequency. With conventional optical fibers, these modes are categorized as bound, guided modes and radiation modes, the latter ones being either evanescent or propagating in character [26]. Of most practical interest are the guided modes and slowly radiating leaky modes.

2.1.2 Solving methods

In this thesis, three approaches for solving the wave equations are used. The first method makes use of analytical trial functions for the longitudinal field components E_z and H_z of a guided mode in a piecewise homogeneous, dielectric fiber profile. The remaining transverse components within each of the homogeneous regions are then retrieved from the relations

$$\mathbf{E}_\perp = \frac{i}{\beta^2 - k_0^2 n^2}(\beta \nabla_\perp E_z - \omega \mu_0 \mathbf{u}_z \times \nabla_\perp H_z), \tag{2.16}$$

$$\mathbf{H}_\perp = \frac{i}{\beta^2 - k_0^2 n^2}(\beta \nabla_\perp H_z + \omega \epsilon_0 n^2 \mathbf{u}_z \times \nabla_\perp E_z), \tag{2.17}$$

which are obtained by making use of Maxwell's curl equations, as well as Eqs. (2.14) and (2.15). Here, the transverse nabla $\nabla_\perp$ operates only in the cross-sectional plane of the fiber and $\mathbf{u}_z$ is a unit vector pointing along the fiber. At the boundary between two neighboring homogeneous regions 1 and 2, the fields are matched by using the continuity relations [27]

$$\mathbf{n} \times (\mathbf{E}_1 - \mathbf{E}_2) = \mathbf{0}, \tag{2.18}$$

$$\mathbf{n} \times (\mathbf{H}_1 - \mathbf{H}_2) = \mathbf{0}, \tag{2.19}$$

where $\mathbf{n}$ denotes a unit vector normal to the boundary. The expressions from each boundary can be collected to a matrix equation

$$\mathcal{M}\mathbf{x} = \mathbf{0} \tag{2.20}$$

where the matrix $\mathcal{M}$ multiplies the trial-function coefficients lumped in the vector $\mathbf{x}$. For the above homogeneous equation, nontrivial solutions can be found whenever the determinant of the matrix $\mathcal{M}$ vanishes. The characteristic equation, $\det(\mathcal{M}) = 0$, is solved numerically to obtain the propagation constant of a mode. This approach is used to solve the guided vector modes in Secs. 3.1 and 3.3.

The second method employs a plane-wave expansion for the field in a spatially periodic, two-dimensional lattice. Such a lattice can act as the cladding in a photonic-bandgap fiber to confine and guide light along an air core. By formulating the

problem in terms of the magnetic field [Eq. (2.11)] instead of the electric field, the transversality condition $\nabla \cdot \mathbf{H} = 0$ can be enforced leading to reduced computational burden [28]. The periodic structure is characterized by a dielectric function with the property $\epsilon_r(\mathbf{r}_\perp) = \epsilon_r(\mathbf{r}_\perp + \mathbf{R}_\perp)$ where $\mathbf{R}_\perp$ is an arbitrary lattice vector. With these assumptions, Bloch's theorem can be invoked to write for the modal field

$$\mathbf{H}(\mathbf{r}) = \mathbf{H}_{\mathbf{k}_\perp}(\mathbf{r}_\perp) \exp[-i(\mathbf{k}_\perp \cdot \mathbf{r}_\perp + \beta z)] \tag{2.21}$$

where $\mathbf{H}_{\mathbf{k}_\perp}$ is a periodic function with the property $\mathbf{H}_{\mathbf{k}_\perp}(\mathbf{r}_\perp) = \mathbf{H}_{\mathbf{k}_\perp}(\mathbf{r}_\perp + \mathbf{R}_\perp)$ and $\mathbf{k}_\perp$ is the Bloch wavevector [28]. By denoting the inverse of the lattice vector $\mathbf{R}_\perp$ by $\mathbf{G}_\perp$, one can expand the periodic part of the field as a sum of plane waves according to

$$\mathbf{H}_{\mathbf{k}_\perp}(\mathbf{r}_\perp) = \sum_{\mathbf{G}_\perp, \kappa} \mathbf{h}_{\mathbf{G}_\perp, \kappa} \exp(-i\mathbf{G}_\perp \cdot \mathbf{r}_\perp) \tag{2.22}$$

where the summation is taken over all vectors $\mathbf{G}_\perp$ for two mutually orthogonal polarization states labeled with $\kappa = 1, 2$ [29]. By using this formalism, the photonic band structures for two-dimensional lattices are computed and the photonic bandgaps permitting optical guidance are identified in Sec. 4.1.

The third method used in this thesis is the finite-element method (FEM). In this method, the computation region is divided into homogeneous subspaces (the finite elements) in which Maxwell's equations are discretized. On the boundaries of the regions, the continuity relations of Eqs. (2.18) and (2.19) are applied [30]. The ensuing set of coupled equations is then numerically solved by means of matrix methods. The FEM is well suited for computing the modes in a lossy waveguide with a perfectly matched layer (PML) as the outer boundary [31]. A properly chosen PML eliminates the reflections from the outer boundary back to the computing region, thus acting as an absorbing boundary. The FEM is used in Sec. 4.2 to investigate the excitation of surface-plasmon polaritons in a metal-coated microstructured optical fiber for sensing applications.

2.1.3 Mode orthogonality and overlap integrals

The bound and radiation modes together form a complete set of functions in the transverse plane of the fiber. In a non-absorbing fiber waveguide, the modes can be normalized to fulfill an orthonormality relation in the form [23, 26]

$$\int (\mathbf{E}_j^* \times \mathbf{H}_k)_z \mathrm{d}^2\mathbf{r}_\perp = \delta_{jk} \tag{2.23}$$

where the indices j and k label the fiber modes and the integration is performed over the transverse plane of the fiber. In such an orthonormal basis, an arbitrary

electromagnetic field can be expanded. In particular, the orthonormality properties can be employed to quantify the power transfer to a specific fiber mode, when a light beam is incident on the end face of the fiber (transverse to the fiber axis). The reflection losses from the end face are usually ignored, and the coupling coefficient to a particular mode is calculated directly from the overlap integral [26]

$$c_j = \int (\mathbf{E}_j^* \times \mathbf{H}_i)_z \mathrm{d}^2\mathbf{r}_\perp \tag{2.24}$$

where $\mathbf{H}_i$ is the magnetic field associated with the incident beam.

For instance, if the incident field is mode-matched to the fundamental guided mode of the fiber, only the corresponding coupling coefficient, say c_0, will be nonzero. In such a case, the excited mode will carry all the incident power. By the same token, the modulus of c_0 is maximized for the given incident power. The mode-matching principles are applied in Secs. 3.1 and 3.3 to quantify the similarities between two optical vector fields in terms of a single number akin to c_0.

2.1.4 Weakly guiding fibers

Cylindrical optical fibers with a small refractive-index contrast between the core and the cladding are said to be weakly guiding [12]. In such waveguides, the modes are uniformly polarized in the cross-sectional plane. Instead of Eq. (2.14), one can proceed by writing for the electric field

$$\widetilde{\mathbf{E}}_j(\mathbf{r}, \omega) = \mathbf{u}_\perp \widetilde{E}_j(\mathbf{r}_\perp, \omega) \exp[-i\tilde{\beta}_j(\omega) z]. \tag{2.25}$$

Here, the field is represented by a scalar amplitude $\widetilde{E}_j$ and $\mathbf{u}_\perp$ denotes a polarization unit vector in the transverse plane of the fiber. The tilde is used to indicate quantities that are exclusive to the weak-guidance approximation (WGA). The magnetic field of the mode is obtained from Eq. (2.3) as

$$\widetilde{\mathbf{H}}_j(\mathbf{r}, \omega) = \epsilon_0 c n(\omega) \mathbf{u}_z \times \widetilde{\mathbf{E}}_j(\mathbf{r}, \omega) \tag{2.26}$$

where the refractive index n is approximated to be equal to that of the core everywhere (zeroth-order WGA) [26]. By normalizing the fields appropriately, the orthonormality relation of Eq. (2.23) can be rewritten for two similarly polarized modes in terms of their scalar electric-field amplitudes as

$$\int \widetilde{E}_j^* \widetilde{E}_k \mathrm{d}^2\mathbf{r}_\perp = \delta_{jk}. \tag{2.27}$$

The overlap integral of Eq. (2.24) can correspondingly be expressed as

$$\tilde{c}_j = \int \widetilde{E}_j^* \widetilde{E}_i \mathrm{d}^2\mathbf{r}_\perp. \tag{2.28}$$

Weakly guided modes are considered in Secs. 3.1 and 3.2. These modes are computed by choosing the trial function for E_z (see Section 2.1.2) to directly stand for the scalar field amplitude $\widetilde{E}_j$, and consequently requiring the radial part and its first derivative be continuous over the cylindrical material boundaries [26].

2.2 Free-space beams

2.2.1 Laguerre–Gaussian beams

The weak-guidance approximation of optical fibers is closely related to the paraxial approximation of free-space propagation. In free space, the wave equation assumes the form

$$\nabla^2\psi(\mathbf{r},\omega) + k_0^2\psi(\mathbf{r},\omega) = 0 \tag{2.29}$$

where ψ describes the amplitude of a scalar field. For propagation along the z-axis, one can write

$$\psi(\mathbf{r}) = u(\mathbf{r})\exp(-ik_0 z). \tag{2.30}$$

In the paraxial approximation, the second derivative of u with respect to z is assumed to be negligible, yielding the paraxial wave equation [32]

$$\nabla_\perp^2 u - 2ik_0\frac{\partial u}{\partial z} = 0. \tag{2.31}$$

Paraxial beams satisfying Eq. (2.31), as well as the weakly guided fiber modes, can be characterized with a small-angle propagation with respect to the optical axis [1].

Among the solutions of the paraxial wave equation are the Hermite–Gaussian modes of a spherical-mirror laser resonator [1]. Another family of solutions is that of the Laguerre–Gaussian (LG) modes for which the spatial part is written in polar coordinates (ρ,θ,z) as

$$u(\mathbf{r}) = f_{l,q}(\rho,z)\exp(-il\theta). \tag{2.32}$$

The first part reads explicitly as [1, 20]

$$\begin{aligned} f_{l,q} &= C_{l,q}\left(\frac{\sqrt{2}\rho}{w}\right)^{|l|}\exp(-\rho^2/w^2)L_q^{|l|}\left(\frac{2\rho^2}{w^2}\right) \\ &\quad\times\exp\{i[(2q+|l|+1)\arctan(z/z_R) - k_0\rho^2/2R]\}, \end{aligned} \tag{2.33}$$

when the following notation is used

$$C_{l,q} = (-1)^q \left(\frac{2}{\pi w^2}\right)^{1/2} \left[\frac{q!}{(|l|+q)!}\right]^{1/2}, \tag{2.34}$$

$$w = w_0(1 + z^2/z_R^2)^{1/2}, \tag{2.35}$$

$$R = z + z_R^2/z, \tag{2.36}$$

$$z_R = w_0^2 k_0/2. \tag{2.37}$$

Here, w_0 denotes the beam-waist parameter, $L_q^{|l|}$ is the associated Laguerre polynomial, the parameter R defines the radius of curvature of the wavefront, and the term $(2q + |l| + 1)\arctan(z/z_R)$ is the Gouy phase. The indices q and l determine the radial and azimuthal orders of the mode, respectively, with the lowest-order case $q = 0$ and $l = 0$ corresponding to the ordinary on-axis Gaussian beam. In general, the transverse intensity profiles of the higher-order LG beams with $l = 0$ ($l \neq 0$) consist of q ($q + 1$) rings surrounding the optical axis [33]. In addition, the helical phasefront of the beams with $l \neq 0$ embody an optical vortex, and thus, they are dark on the optical axis [34]. Experimentally, the higher-order LG beams could be produced directly within a laser cavity, but in practice they are often generated from the standard Hermite–Gaussian laser beams outside the cavity by using, e.g., cylindrical-lens converters [35]. Another popular conversion technique employs a spatial light modulator to introduce the helical, azimuthal phase twist of Eq. (2.32) into a Gaussian beam [33, 36]. LG beams are considered in Sec. 3.2 and in Ch. 5.

2.2.2 Optical angular momentum

The cycle-averaged linear-momentum density of an electromagnetic field can be calculated from the expression [21]

$$\mathbf{p} = \frac{1}{c^2}\langle \mathbf{S} \rangle \tag{2.38}$$

where the cycle-averaged Poynting vector is given by

$$\langle \mathbf{S} \rangle = \frac{1}{2}\mathrm{Re}(\mathbf{E} \times \mathbf{H}^*). \tag{2.39}$$

In analogy to classical mechanics, the angular-momentum density of the field is determined by the cross product [37]

$$\mathbf{j} = \mathbf{r} \times \mathbf{p}. \tag{2.40}$$

Higher-order helical beams ($l \neq 0$) of the form of Eq. (2.32) carry orbital angular momentum, which is manifested by a non-vanishing z-component of the corresponding angular-momentum density. Explicitly, the z-component for a linearly polarized LG mode is obtained as [38]

$$j_z = \epsilon_0 \omega l |f_{l,q}|^2. \tag{2.41}$$

In addition to the above orbital contribution, one can associate the polarization state of the beam with spin angular momentum. For example, if one denotes the left- and right-handed circular polarization states with $\sigma_z = \pm 1$, the ratio of the total angular-momentum flux and the energy flux (per unit length) can be obtained as [38]

$$\frac{J_z}{cP_z} = \frac{\int j_z \mathrm{d}^2\mathbf{r}_\perp}{c \int p_z \mathrm{d}^2\mathbf{r}_\perp} = \frac{l + \sigma_z}{\omega} \tag{2.42}$$

where the quantity P_z is the z-component of the momentum and the integrations are performed over the transverse plane.

Equation (2.42) expresses the total angular momentum flux in terms of the orbital and spin contributions. This very sum term turns out to be responsible for the spectral shifts that occur when the optical field and an observer are in relative rotational motion about the optical axis [39]. In Ch. 5, such rotational shifts are considered, for the first time, for optical fields which are only partially coherent.

2.2.3 Partially coherent beams

Thus far, completely coherent, monochromatic fields have been considered. In reality, however, random fluctuations are always present in light [1]. The coherence properties of a random, uniformly polarized, stationary optical beam can be described by the mutual coherence function [40]

$$\Gamma(\mathbf{r}, \mathbf{r}'; \tau) = \left\langle \psi^*(\mathbf{r}, t) \psi(\mathbf{r}', t') \right\rangle. \tag{2.43}$$

Here, $(\mathbf{r}, t)$ and $(\mathbf{r}', t')$ denote two space-time points, and the explicit introduction of the variable $\tau = t - t'$ indicates the stationarity of the field. Furthermore, the angle brackets denote the ensemble average of all possible field realizations. The spectral coherence properties are described by the cross-spectral density function which is obtained by using the (generalized) Wiener-Khintchine theorem [40]

$$W(\mathbf{r}, \mathbf{r}', \omega) = \frac{1}{2\pi} \int_{-\infty}^{\infty} \Gamma(\mathbf{r}, \mathbf{r}', \tau) \exp(i\omega\tau) \mathrm{d}\tau. \tag{2.44}$$

A convenient tool for the investigations in the realm of optical coherence is the coherent-mode representation of the cross-spectral density function [40]. Accordingly, a complete set of basis functions, such as the free-space LG modes [41], can be employed to write

$$W(\mathbf{r},\mathbf{r}',\omega)=\sum_{l=-\infty}^{\infty}\sum_{q=0}^{\infty}\lambda_{l,q}(\omega)\psi_{l,q}^{*}(\mathbf{r},\omega)\psi_{l,q}(\mathbf{r}',\omega). \tag{2.45}$$

In this summation, each term represents a fully coherent mode in the space-frequency domain [40]. The coherent-mode representation is put to use in Ch. 5.

Chapter 3

Guided modes in hollow-core and annular-core optical fibers

In this chapter, mode-analysis techniques are applied to hollow-core and annular-core fibers. The accuracy of the weak-guidance approximation is first assessed by considering some low-order modes [Paper I]. Then, the approximation is employed to investigate the use of hollow-core multimode fibers as evanescent-wave conveyor tubes for laser-cooled atoms in two configurations; by selectively exciting tubular fiber modes with Laguerre–Gaussian beams and by dithering a Gaussian beam at the fiber input to average out the speckles due to multimode interference [Paper II]. Finally, the Talbot effect related to annular-core fibers is analyzed by using the full-vector mode description [Paper III].

3.1 Weakly guided modes vs. exact vector modes

The majority of optical fibers in use today, e.g., in the global telecommunication network, are composed of pure and doped silica glass [1]. Thus, the fibers typically exhibit only small refractive-index contrasts in their transverse profiles legitimating modal analysis in the weak-guidance approximation (WGA) [12]. The uniform polarization state of the weakly guided modes is usually taken to be linear in the transverse plane of the fiber. Since most of the laser beams are uniformly polarized [42], the field patterns of such linearly polarized (LP) modes are commonly encountered when light is coupled to fibers. Of course, the excited field will always comprise a superposition of the actual (hybrid) vector modes [43]. Incidentally, the WGA can be successfully used outside its apparent regime of validity, as in correctly yielding the propagation constants of all transverse electric (TE) modes [26].

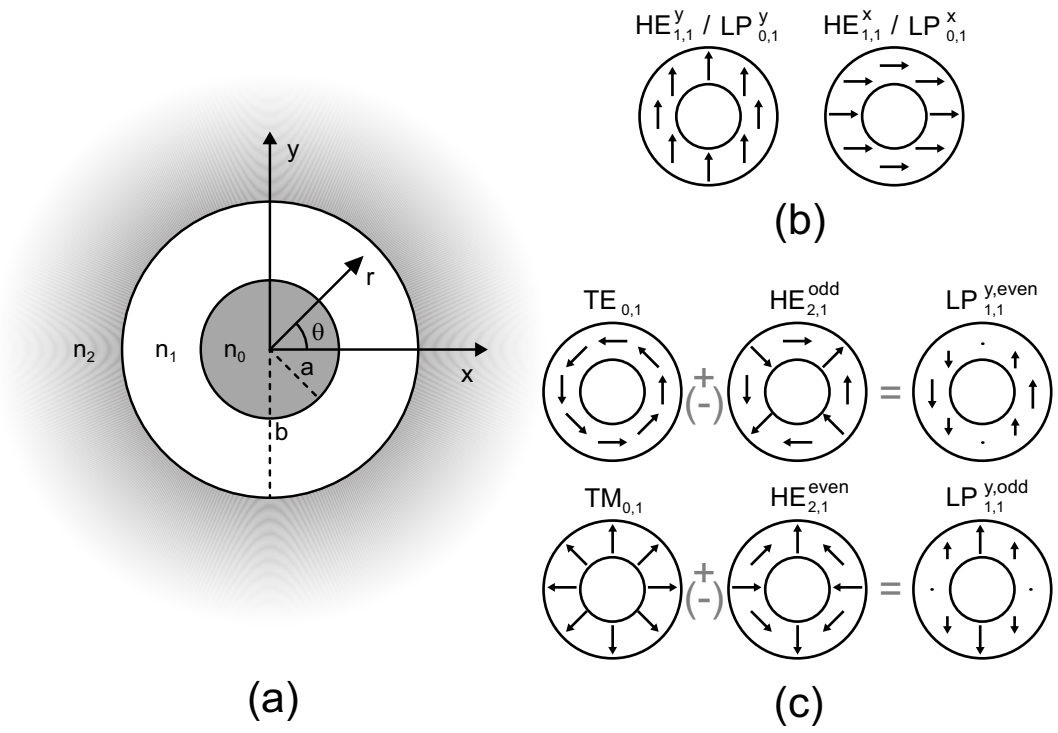

Figure 3.1: (a) Schematic cross-section of annular-core and hollow-core optical fibers with a and b denoting the inner and outer radii of the core, respectively. The refractive index of the core, n_1, is higher than the indices of the inner and outer claddings, n_0 and n_2, respectively. (b) Polarization patterns of the fundamental $\mathrm{HE}_{1,1}$ mode and the corresponding linearly polarized $\mathrm{LP}_{0,1}$ mode. (c) Emergence of the second-order $\mathrm{LP}_{1,1}$ modes as a superposition of the corresponding vector modes.

In addition to the refractive-index contrasts, the transverse fiber geometry may also affect the accuracy of the WGA.

The cross-sectional fiber geometry of annular-core and hollow-core optical fibers is schematically shown in Fig. 3.1(a). In an annular-core optical fiber (ACF), the refractive index in the inner cladding equals that of the outer cladding ($n_0 = n_2$), whereas in a hollow-core optical fiber (HOF), the inner cladding is missing ($n_0 = 1$). The modal fields in these fibers are similar to the ones in a conventional step-index fiber, apart from a reduced intensity in the region enclosed by the core [44, 45]. Accordingly, the fundamental $\mathrm{HE}_{1,1}$ mode is represented by the $\mathrm{LP}_{0,1}$ mode in the WGA [26]. Both of these modes are two-fold degenerate, and their generic polarization patterns are schematically depicted in Fig. 3.1(b). The $\mathrm{LP}_{1,1}$ mode, on the other hand, corresponds to an equal-weight superposition of the odd (even) $\mathrm{HE}_{2,1}$ mode and the $\mathrm{TE}_{0,1}$ ($\mathrm{TM}_{0,1}$) mode [26], as visualized in Fig. 3.1(c). By taking

into account the possible combinations of the vector modes, the $\mathrm{LP}_{1,1}$ mode is seen to be altogether four-fold degenerate. Moreover, the amplitude of this mode has a sinusoidal azimuthal variation.

In a weakly guiding fiber with the property $n_1 - n_2 \ll 1$, the modes are often calculated by using the WGA. On the face of it, this would seem to be justified only for ACFs, but the approach has proven to work well also for some HOFs [44, 45]. To establish the range of geometry and material parameters for which the WGA will yield accurate results, the overlap integral of Eq. (2.24) is brought into service. By taking the magnetic field in this integral to be that of the LP mode [from Eq. (2.26)] and the electric field to be the corresponding vector mode (or the appropriate superposition), one can quantify how well the two modal fields are matched. Since only the electric-field components parallel to the polarization direction of the LP mode remain in the integrand, one can equivalently consider a projection integral by writing

$$|\widetilde{W}|^2 = \left| \int \mathbf{E}^* \cdot \widetilde{\mathbf{E}} \mathrm{d}^2\mathbf{r}_\perp \right|^2 \leq 1. \tag{3.1}$$

Here, the upper bound of unity is due to the following normalizations

$$\int |\mathbf{E}|^2 \mathrm{d}^2\mathbf{r}_\perp = \int |\widetilde{E}|^2 \mathrm{d}^2\mathbf{r}_\perp = 1, \tag{3.2}$$

and it corresponds to the case where the two fields are exactly matched. The value of $|\widetilde{W}|^2$ is reduced below unity whenever the electric-field patterns differ in amplitude and/or polarization. In fact, by including the non-vanishing z-component of the exact vector field in the normalization integral, the case $|\widetilde{W}|^2 = 1$ can be approached only asymptotically.

In paper I, the above overlap-integral formalism is applied to weakly guiding ACFs and HOFs with the following rule-of-thumb findings: For ACFs, the WGA describes the low-order modes well for core thicknesses much above (or much below) the optical wavelength. For HOFs, on the other hand, the core needs be thicker than roughly half the outer radius of the core for the WGA to be valid. The quantity $|\widetilde{W}|^2$ is in general closer to unity for the second-order modal fields than for the fundamental fields. Furthermore, the discrepancies between the approximate and exact fields are emphasized if the transverse core dimensions are large or if one operates near a modal cutoff. Naturally, the weaker the guidance in terms of the refractive-index contrast, the more functional the approximation. Moreover, by letting the value of n_0 vary, the parameters for single-mode guidance can most accurately be obtained in the WGA if the ratio a/b has a high value, i.e., if the core is thin.

3.2 Spatially smooth fields within a multimode hollow-core fiber

The electromagnetic fields of a HOF can be exploited in confining and guiding small, polarizable particles in the empty pore by means of optical forces. For a uniformly polarized, spatially inhomogeneous field, the complex amplitude of Eq. (2.5) can be separated into amplitude and phase contributions as [24]

$$\mathbf{E}(\mathbf{r}) = E_0(\mathbf{r}) \exp[i\phi(\mathbf{r})]\mathbf{u}_E \tag{3.3}$$

where E_0 and ϕ are assumed to be real-valued functions and $\mathbf{u}_E$ is the polarization vector. The dipole moment induced on a dipole-like particle in the field is [32]

$$\boldsymbol{\mu} = \alpha\mathbf{E} \tag{3.4}$$

where $\alpha = \alpha' + i\alpha''$ is the complex polarizability. By using this notation, the cycle-averaged force acting on the particle can be cast into the form [24]

$$\langle \mathbf{F} \rangle = \frac{\alpha'}{4}\nabla E_0^2 + \frac{\alpha''}{2}E_0^2\nabla\phi. \tag{3.5}$$

The first component in Eq. (3.5) corresponds to the gradient force which either attracts the particle toward regions of high intensity ($\alpha' > 0$) or repels the particle from such regions ($\alpha' < 0$). The second force component is the scattering force which originates from the momentum transfer from the field to the particle.

The attractive gradient force can be employed in particle guiding by exciting the leaky $\mathrm{EH}_{1,1}$ mode which has an on-axis intensity maximum in the pore of a HOF. Consequently, the particles with sufficiently small transverse velocities are held near the optical axis far away from the fiber wall. This mechanism has been used to demonstrate, e.g., direct-write lithography [46] and the transfer of laser-cooled atoms from one vacuum chamber to another [47]. However, the guiding distance in this scheme is limited by the inherent decay of the mode amplitude. Also, when dealing with cold atoms, the heating effect due to the scattering force can become crucial [48]. To overcome these issues, the repulsive gradient force associated with the evanescent wave of a core-guided optical field can instead be used. Since the evanescent wave of such a field is strongly localized near the fiber wall, the atoms will spend most of their time in the dark near the optical axis. In principle, the tubular fundamental field of a single-mode HOF would lend itself perfectly to the task, but in practice, multimode HOFs are resorted to owing primarily to their much larger openings. The basic problem with the use of multimode HOFs is the speckle due to multimode interference [49]. As a consequence, there will be dark and faint spots on the fiber wall, which decimates the flux of guided atoms by way of their

van der Waals interaction with the fiber [50]. In what follows, two methods for obtaining a smooth evanescent-wave field on the inner surface of a weakly guiding multimode HOF are analyzed [Paper II]. The example fiber parameters for the calculations are chosen so that the WGA can be adopted.

The first method relies on the notion that a superposition of the even and odd variant of a higher-order $\mathrm{LP}_{m,p}$ mode with a relative $\pi/2$ phase difference will lead to an azimuthally flat intensity distribution. This can be verified, e.g., by superposing the even and odd $\mathrm{LP}_{1,1}$ modes of Fig. 3.1(c). The resulting modal field will then have a helical azimuthal phase dependence of the form $\exp(-im\theta)$ reminiscent of the Laguerre–Gaussian mode in Eq. (2.32). If circularly polarized light is used, such a helical field can be made to propagate in an invariant manner even when the WGA is not valid [43, 51]. According to the overlap integral of Eq. (2.28), a normal-incidence LG beam would exclusively couple to fiber modes that have the same helical twist, i.e., to the modes for which $m = l$. When individually excited, the helical fiber mode will provide a spatially uniform evanescent-wave field on the fiber wall. Additionally, the optical axis will remain dark outside the fiber when beams with $l \neq 0$ are used, which should be an advantage for loading and unloading of the atoms. An atom guiding scheme based on this approach is sketched in Fig. 3.2(a).

If the HOF supports higher-radial-order $\mathrm{LP}_{m,p}$ modes (with $p > 1$) for a given value of the azimuthal index m, the selection between them can be carried out by adjusting the beam-waist parameter w_0 of the LG beam. This is exemplified in Fig. 3.3(a) which shows the highest relative intensities attainable on the inner surface of a HOF as a function of the azimuthal mode index l (or m) of an incident LG beam carrying unit power. The radial LG-beam order, q, is shown above each data point, and the underscore marks the excitation of an LP mode with a higher radial number, i.e., with $p = 2$ for this particular fiber. In all other cases, the $\mathrm{LP}_{m,1}$ mode is the excited one. Also plotted is the squared modulus of the coupling coefficient of Eq. (2.28), i.e., the fraction of the incident power carried by the mode. From the figure, one can note that the highest intensity values originate from the excitation of the $\mathrm{LP}_{m,2}$ modes, whereas the excitation efficiency can be very high for a higher-order $\mathrm{LP}_{m,1}$ mode.

The second method, sketched in Fig. 3.2(b), makes use of a rapid variation of the incident angle of a Gaussian input beam in the time scale of the atomic motion [52]. At a given time instant, several fiber modes will be excited, which gives rise to a multimode speckle. Dithering of the incident angle in time leads to a constantly varying speckle pattern which, from the standpoint of cold, slowly moving atoms, manifests itself as a smooth, time-averaged field. The principle is similar to that of the time-averaged, orbiting-potential (TOP) method used in the first observation of Bose–Einstein condensation [53], or to that of the rotating-beam ROBOT trap [54].

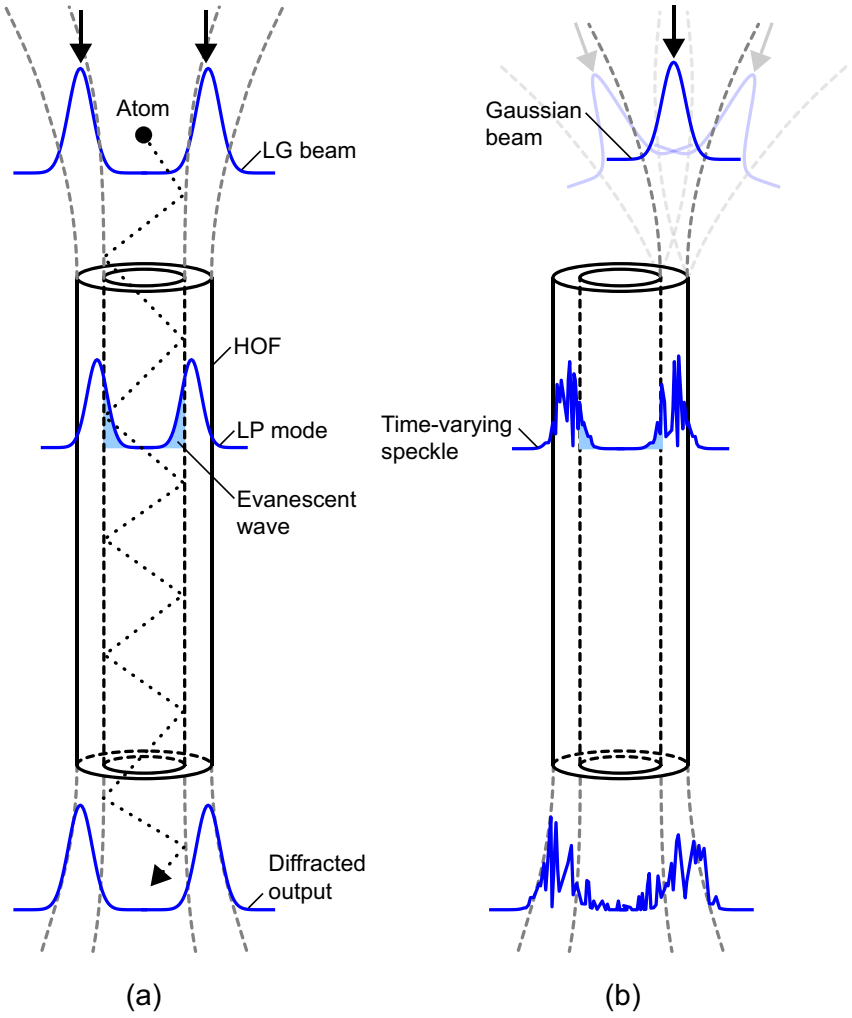

Figure 3.2: Atom guiding through hollow-core optical fibers (HOFs). (a) Laguerre–Gaussian (LG) beam excites a helical, linearly polarized (LP) fiber mode which provides a spatially uniform evanescent wave on the fiber wall. (b) Similar conditions on the fiber wall can be produced by dithering the incident angle of a Gaussian beam at the fiber input, as first suggested in Ref. [52].

The field on the fiber wall needs to be obtained by numerical means, since its direct observation would be cumbersome. By denoting the angles with respect to the optical axis by α and γ [perpendicular and parallel to the plane of Fig. 3.2(b), respectively], one can construct the spatial speckle profile on the fiber wall as a function of the input-beam angle by using Eq. (2.28). The maximum angle is taken to be equal to the numerical aperture of the fiber. The sum of the calculated multimode intensity profiles divided by their count results in a profile that corresponds

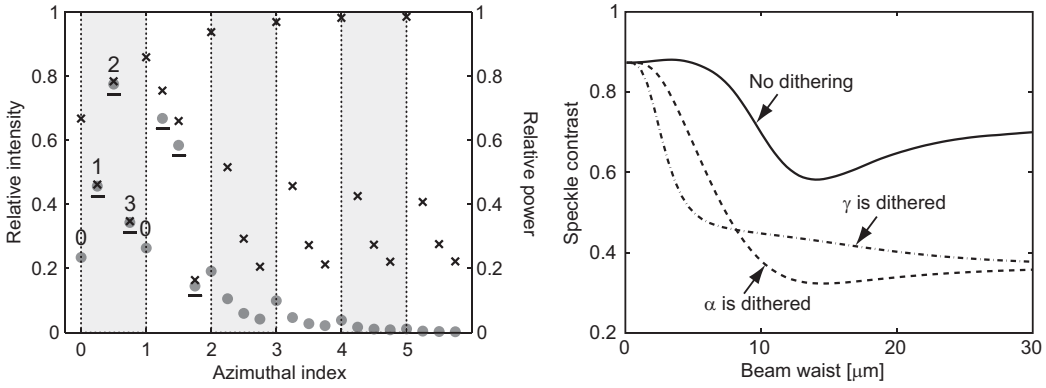

Figure 3.3: (a) Highest attainable intensity on the fiber wall as a function of the azimuthal mode index for LG beams with radial indices $q = 0, \ldots, 3$ (dots). The underscore indicates the excitation of a higher-order $\mathrm{LP}_{m,2}$ mode. Also shown is the relative amount of power in the mode (crosses). (b) Contrast of the speckle pattern on the fiber wall when the input-beam angle is dithered in two mutually orthogonal directions. For reference, the undithered case is also shown. [Paper II]

to a time-average over all profiles. The granularity of this time-averaged intensity profile on the fiber wall is characterized by its contrast defined as

$$C_{sp} = \sigma_I / \langle I \rangle \tag{3.6}$$

where σ_I denotes the standard deviation in the pattern and $\langle I \rangle$ is the average intensity. By assuming that a Gaussian beam is incident on the center of the rim of the fiber core, the contrast values given in Fig. 3.3(b) are obtained as a function of the incident-beam waist. Also shown is the static case for a normal-incidence beam without the dithering. After studying a number of multimode HOFs with thicker cores, and thus with more supported guided modes, it was observed that the dithering of the angle α always yields the smoothest optical wave on the fiber wall.

3.3 Self-imaging in annular-core fibers

A laterally periodic solution to the paraxial free-space wave equation of Eq. (2.31) will be periodic also in the propagation direction. This phenomenon is known as the self-imaging effect, or the Talbot effect, and it can be encountered in an approximate form with cylindrical multimode waveguides. In particular, annular-core fibers (ACFs) naturally provide periodicity in the azimuthal direction. Thus, one often approximates the field in such a waveguide as being a wrapped-around equivalent of

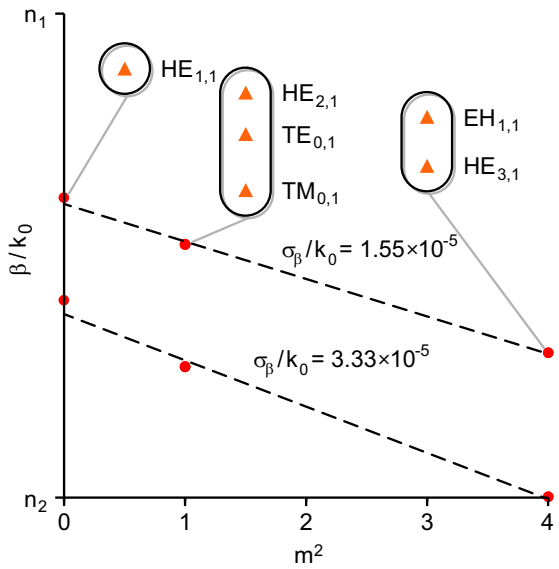

Figure 3.4: Normalized propagation constants β/k_0 of the vector modes arranged according to the index m of the $\mathrm{LP}_{m,1}$ modes (dots). The insets illustrate that for $m > 1$ there are two modes (three modes for $m = 1$) with almost degenerate propagation constants (triangles). Dashed lines are least-squares fits with σ_β denoting their standard deviations. [Paper III]

a one-dimensional, laterally periodic field. Based on this analogy, an ACF with a thin core appears to be the best choice for the self-imaging applications [14–16]. However, as indicated in Sec. 3.1, the scalar, weak-guidance approximation behind this reasoning tends to break down in particular for such waveguides.

To investigate the applicability of the ACFs for self-imaging, the vector modes of the fiber are grouped according to their WGA counterparts which, for the low-order modes, are indicated in Figs. 3.1(b) and (c). Figure 3.4 illustrates how the propagation constants of the vector modes then place themselves as a function of m^2 in two weakly guiding, single-radial-mode example ACFs. The propagation constants of the $\mathrm{LP}_{m,1}$ modes of such ACFs approximately obey the quadratic dependence [15]

$$\tilde{\beta} = \tilde{\beta}_0 - \tilde{\beta}_1 m^2 \tag{3.7}$$

where $\tilde{\beta}_0$ and $\tilde{\beta}_1$ are positive constants. If the relation given in Eq. (3.7) was strictly obeyed, a superposition of the modal fields at the plane $z = 0$ would be perfectly imaged to the plane located at the Talbot distance, given by

$$z_T = 2\pi/\tilde{\beta}_1, \tag{3.8}$$

with the phase factor of each mode being equal to $\exp(-i\tilde{\beta}_0 z_T)$. Thus, by determining how well the vector modes obey this same quadratic dependence, one can evaluate the self-imaging capability of an ACF. For this purpose, a straight line is fitted [from Eq. (3.7)] to the propagation-constant data, as illustrated by the dashed lines in Fig. 3.4. The slope of the line will then yield the Talbot distance, as in Eq. (3.8), while the standard deviation of the data points, σ_β, will be used to quantify the general self-imaging capability from the plane $z = 0$ to the plane $z = z_T$.

The above fitting approach is applied to weakly guiding ACFs in Paper III. The results indicate that, as a trend, the general self-imaging potential weakens in terms of the fitting deviation when the core is made thicker. This potential is also weakened when the radius of the core is made larger for a fixed value of the core thickness in order to increase the number of modes available in the imaging. In particular, a mode just above its cutoff strongly deteriorates the fit, as evidenced by the lower data set in Fig. 3.4. The example cases considered in Paper III make use of the overlap integral of Eq. (3.1) to compare the original vector field and its image.

Chapter 4

Microstructured optical fibers with coated inclusions

The technology for manufacturing microstructured optical fibers with an array of holes in their transverse profiles is nowadays well established [55, 56]. When filled with liquids or gases, the fibers can be employed in various sensing configurations [57]. Furthermore, the use of coated, solid-state inclusions within the fiber holes has aroused interest, as this opens up perspectives for compact, fiber-integrated optoelectronic devices [19] and sensors [58–60].

In this chapter, two numerical studies related to the research of coated microstructured optical fibers are summarized. First, the effect of a dielectric, high-index coating on the transmission band of an air-guiding, photonic-bandgap fiber is characterized. Second, a novel design for a surface-plasmon-resonance sensor for aqueous analytes is proposed [Paper IV]. The sensor design is based on a three-hole microstructured optical fiber with metal-coated hole surfaces.

4.1 Photonic-bandgap fibers with dielectric high-index inclusions

The light-guiding mechanism of a photonic-bandgap fiber (PBF) is based on the photonic-bandgap effect caused by a spatially periodic cladding structure [61]. Since the total internal reflection is not employed, even an empty region surrounding the optical axis can function as the fiber core. However, only the wavelengths that fall within the full, transverse bandgap of the fiber cladding can efficiently be guided. A typical PBF is made of silica glass with the cladding holes arranged in a triangular formation in the cross-sectional plane of the fiber [8]. The spectral width of the

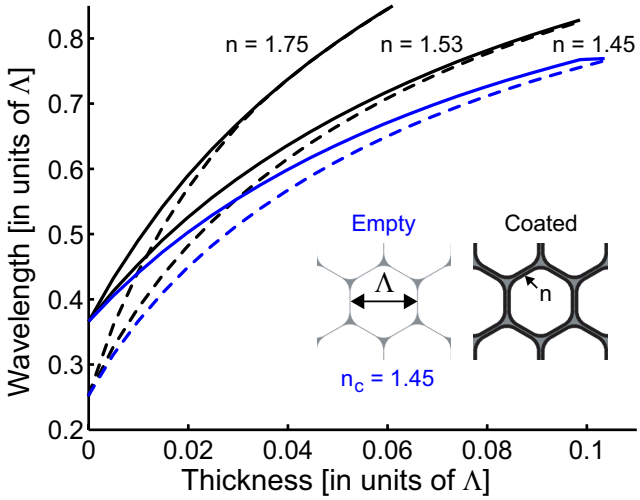

Figure 4.1: Bandgap-edge wavelengths as a function of the coating thickness for three values of the coating refractive index. Inset: Cross-section of the original fiber cladding and one with coated inclusions.

transmission bandgap can be increased by increasing the air-filling fraction in the cladding [62]. With high enough air-filling fractions, the holes assume a strongly hexagonal form in the triangular lattice. In what follows, the effect of uniform, dielectric, high-index coated inclusions on the (main) photonic bandgap of such a fiber is characterized. The fiber is assumed to be made of silica glass with a refractive index of $n_c = 1.45$ and an air-filling fraction of $f = 0.95$.

The photonic bands of the cladding are calculated by using a freely available implementation of the plane-wave expansion method [63, 64] outlined in Sec. 2.1.2. By scanning through the Γ, M, and K points of the first irreducible Brillouin zone associated with the triangular lattice [28], one obtains the photonic band structure for a fixed value of the propagation constant β. From the band structure, the frequencies that lie within a full, transverse photonic bandgap are then retrieved. This procedure is repeated for each value of β. In order to guide light along the fiber core by exploiting the bandgap effect, the dispersion curve of the core material has to intersect with the obtained bandgaps in the $\beta\omega$-plane [2]. Figure 4.1 shows the wavelengths at the intersection points, i.e., at the actual bandgap edges for air guidance as a function of the coating thickness [65]. The dielectric profile of the fiber cladding is depicted in the inset with Λ denoting the hole-to-hole distance. Three pairs of curves are shown for different values of the refractive index n of the coating, including for reference the case where both the coating and the fiber material are taken to be silica ($n = n_c$) [62].

From the figure, one can note that the bandgap shifts to longer wavelengths and narrows when the coating is made thicker. These features are more pronounced with the higher-index the coating materials. Typical values of Λ are on the order of a couple of microns, and thus, even a few nm layer on the hole surfaces can perceivably alter the spectral position (and width) of the original bandgap.

4.2 Surface-plasmon-resonance sensor based on microstructured fiber with metal inclusions

In recent experimental demonstrations, the micron-size holes of a microstructured optical fiber (MOF) have successfully been coated with gold [19] and silver [66,67]. When the right conditions are met, the interfaces between the metallic and dielectric domains in the fiber support the propagation of surface-plasmon polaritons [68]. These electromagnetic surface waves are associated with collective electronic oscillations [69], and they have two important characteristics that are particularly useful for sensing applications. First, the plasmon is strongly localized near the interface [70], which contributes, e.g., to surface-enhanced Raman scattering (SERS) [71, 72]. Second, the wavelength for which the plasmon excitation is at its strongest, i.e., the resonance wavelength, will sensitively depend on the dielectric in contact with the metal [73, 74].

By taking a MOF with metal-coated pore surfaces, one can construct a highly compact, fiber-integrated surface-plasmon-resonance sensor by infiltrating a liquid analyte into the empty pores. In such configurations, light propagating in the fiber core excites a surface-plasmon polariton at the metal-analyte interface. For a given metal structure, the plasmon-resonance characteristics are dictated by the refractive index of the analyte. Several sensor designs based on these concepts have been proposed so far [58–60]. However, all of them require selective coating and filling of tiny, micron-size cladding holes. Also, the loss level of these devices could not be tuned without affecting the spectral signature of the plasmon resonance.

In this thesis, a novel sensor design is put forward to overcome these drawbacks [Paper IV]. The starting point here is a three-hole MOF, such as the one shown in Fig. 4.2(a). This template fiber can be converted into a sensor device by first coating the hole surfaces with an auxiliary low-index dielectric layer on top of which a thin gold layer is deposited. The cross-section of the resulting structure is schematically depicted in Fig. 4.2(b). The parameters s (n_s), h (n_h), and d (n_d) denote the thicknesses (refractive indices) of the auxiliary dielectric layer, the core strut, and the gold layer, respectively. The analyte filling the pores is assumed to be water-based with a refractive index of $n_a \approx 1.33$. Furthermore, the parameter r denotes

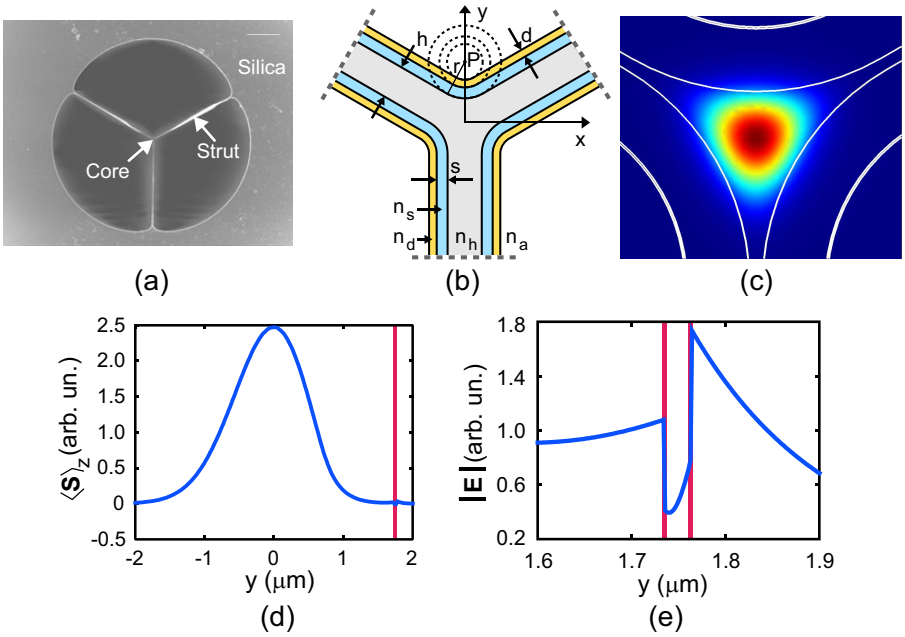

Figure 4.2: (a) Micrograph of a three-hole MOF [75]. (b) Parameters in the layered sensor design. (c) Longitudinal component of the time-averaged Poynting vector for the Gaussian guided mode. (d) Vertical cut of the mode profile plot. (e) Close-up of the norm of the electric field in the vicinity of the gold layer. Red vertical lines mark the locations of the gold-layer interfaces. [Paper IV]

the radius of curvature from point P which locally dictates the growth direction of the layers [19]. In the proposed approach, all three fiber holes can be coated and later filled with the analyte simultaneously. The hole sizes can be taken as large as practically possible to facilitate the coating and filling processes. Recently, strut lengths on the order of tens of microns have been reported [76]. Most importantly, the thickness parameter s of the auxiliary dielectric can be used to exclusively tune the loss level of the sensor by controlling the overlap between the core-confined mode and the gold layer.

The modal fields of the structure are calculated by using the FEM discussed in Sec. 2.1.2. A commercial software is employed in the calculations [77]. Among the obtained solutions, the spatially Gaussian ones are sought, since at each wavelength an incident Gaussian beam would most efficiently couple to such modes. The Gaussian mode of the device is doubly degenerate within the accuracy of the computations, and its spatial characteristics are illustrated in Figs. 4.2(c)-(e). Figures 4.2(c) and (d) show the z-component of the time-averaged Poynting vector, and Fig. 4.2(e) illustrates the local behavior of the field amplitude near the gold

layer. The spatially decaying character of a plasmon is apparent in Fig. 4.2(e), and the propagation losses of the mode are thus attributed to the excitation of a surface-plasmon polariton.

The decay of the optical power of the Gaussian mode is governed by the imaginary part of the propagation constant through the relation [22]

$$\alpha_L = 2\mathrm{Im}(\beta). \tag{4.1}$$

By considering the loss as a function of the optical wavelength for two different analytes, the sensitivity of the sensor fiber can be assessed. According to a conservative estimate, refractive-index changes on the order of 1×10^{-4} can be detected with the device. Fortunately, this figure is obtained when the refractive-index contrast between the auxiliary layer and the fiber core is made small, which should enable single-core-mode operation with fibers having a sufficiently small core. Instead of gold, copper could in principle be used as it exhibits very similar plasmon-resonance characteristics.

Chapter 5

Rotational frequency shifts in partially coherent optical fields

In addition to linear momentum, light can also carry optical angular momentum [78]. In analogy to atomic physics, this is often separated into spin and orbital angular-momentum contributions which are associated with the polarization state and the phasefront of a light beam, respectively [78]. A circularly polarized beam propagating along the z-axis carries spin angular momentum of $\sigma_z\hbar$ per photon with $\sigma_z = \pm 1$ denoting the two orthogonal states of circular polarization and $\hbar$ being the Planck constant divided by 2π. Beams with helical phasefronts of the form $\exp(-il\theta)$, such as the LG beams of Eq. (2.32), additionally carry orbital angular momentum of $l\hbar$ per photon [1, 20]. The mechanical equivalence of the spin and orbital parts has experimentally been established by transferring optical angular momentum to a weakly absorbing particle trapped with optical tweezers [79]. The tweezers comprise a tightly focused beam whose ability to capture and trap the particle can be understood by means of the attractive gradient force [80]. As demonstrated in this micromanipulation experiment, it is the total optical angular-momentum content of the beam per photon, $(l + \sigma_z)\hbar$, that is responsible for the torsional action on the particle.

Another phenomenon intimately tied to the total optical angular-momentum content of a light beam is the rotational frequency shift. This shift can be observed in the direction of the rotation axis, and thus, it is distinct from the translational Doppler effect. In quantitative terms, the angular frequency of a helical beam is shifted by the amount $(l+\sigma_z)\Omega$ where Ω is the angular frequency of rotation (about the optical z-axis) between the field and the observer [39]. Since the LG beams comprise a complete set of basis functions, any beam can be expanded in terms of these functions. Indeed, the shifts have been used to determine the relative weights of the helicity components of a light beam [81], also at the single-photon level [82].

The shifts have also been used in creating moving interference patterns for optical micromanipulation [83]. In a similar vein, the guided atoms within a hollow-core optical fiber considered in Sec. 3.2 experience a shifted optical frequency due to their azimuthal motion [84]. In this thesis, the rotational shifts are for the first time considered in the context of partially coherent fields [Paper V].

In the theory of optical coherence, one formally deals with an ensemble of field realizations [1, 40]. A realization of a uniformly polarized field propagating toward the positive z-direction can be expanded in terms of the LG modes. Here, the amplitudes of the basis modes are taken to be randomly fluctuating functions of time with zero mean. The rotational motion between the field and the observer about the z-axis can be treated with a simple coordinate transformation [85]. In effect, the azimuthal coordinate for each basis mode becomes a function of time according to

$$\theta(t) \rightarrow \theta - \Omega t. \tag{5.1}$$

By making this substitution to the field realizations, and writing the expression for the mutual coherence function in the space-time domain [Eq. (2.43)], one can make the following general observations: The angular frequency of each basis mode will be shifted by the amount $(l + \sigma_z)\Omega$ as expected. As a consequence, even a field which is stationary for $\Omega = 0$ can become nonstationary for $\Omega \neq 0$. This behavior will occur whenever the modes with different azimuthal indices l, and thus with differently shifted optical frequencies, are at least partially correlated.

The above formalism is exemplified in Paper V by considering a superposition of completely uncorrelated LG basis modes. The resulting field will then be stationary also for the case $\Omega \neq 0$, and one can proceed as in Sec. 2.2.3 to calculate the cross-spectral density function from the coherence function through Eq. (2.44). For the field at rest, i.e., for $\Omega = 0$, Gaussian Schell-model spatial correlations and a Lorentzian spectrum centered at the angular frequency ω_0 are assumed. With these assumptions, the cross-spectral density function for the case $\Omega \neq 0$ can be derived in the form of a coherent-mode representation. From this expression, the spectral density is explicitly obtained as

$$\begin{aligned} S(\mathbf{r}, \omega; \Omega) &= \left(\frac{2}{\pi w_G^2}\right) \exp[-2\eta^2(1+\xi^2)] \\ &\quad \times \sum_{l=-\infty}^{\infty} I_{|l|}(2\xi^2\eta^2) g[\omega - \omega_0 - (l+\sigma_z)\Omega]. \end{aligned} \tag{5.2}$$

Here, w_G is the beam-waist parameter, $\eta = r/w_G$ is the normalized radial coordinate, $I_{|l|}$ is the modified Bessel function of the first kind of order $|l|$, and g is a Lorentzian spectral profile centered at $\omega_0 + (l + \sigma_z)\Omega$. The parameter ξ describes the global spatial coherence properties of the field; for a completely coherent field

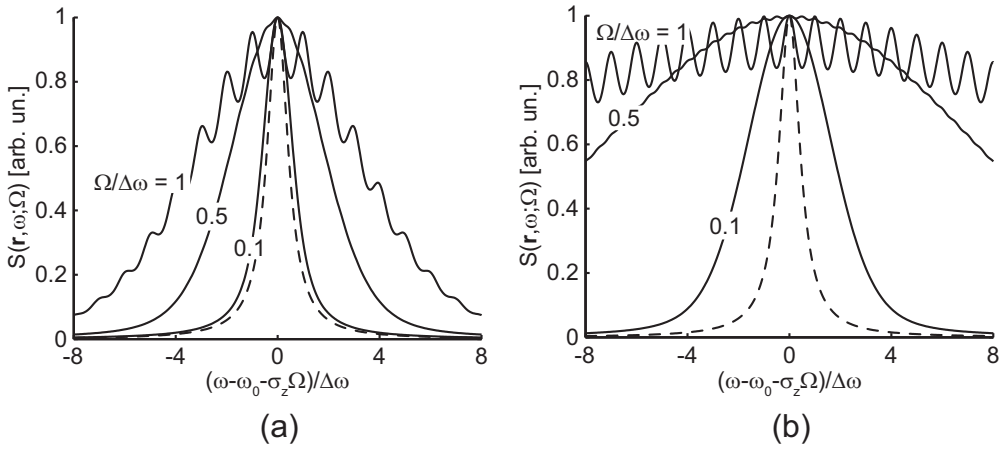

Figure 5.1: Spectral density for different rotation frequencies Ω with weight functions (a) $I_{|l|}(10)$ and (b) $I_{|l|}(200)$. The Lorentzian lineshape function of width $\Delta\omega$ is shown in dashed line. All the curves are normalized to have the peak value of unity. [Paper V]

$\xi = 0$ and for a completely incoherent field $\xi \to \infty$. Thus, the more incoherent the field, the more terms in the summation of Eq. (5.2), and consequently, the more diverse the spectral effects due to the rotation. This same qualitative argument applies to observation points far from the optical axis, as the parameter η will equally affect the summation.

Figure 5.1 illustrates the effect of rotation on the spectrum for two argument values of the terms $I_{|l|}(2\xi^2\eta^2)$ in Eq. (5.2). In both of the plots, the overall spectral width is seen to increase along with the value of Ω. Also, with high enough rotation frequencies, the peaks of the individual Lorentzians appear separately. For a fixed value of η, one can consider the differences between Figs. 5.1(a) and (b) to manifest changes in the state of spatial coherence through the parameter ξ. Vice versa, for a fixed value of ξ, these differences manifest changes in the observation distance η.

Chapter 6

Summary and discussion

Various specialty optical fibers are widely used in many branches of science and technology. Novel fiber-optical components are often designed with numerical tools, because ample computational resources are nowadays readily available. In this thesis, analytical and numerical mode-analysis techniques are applied to layer-structured optical fibers and partially coherent optical fields. More explicitly, these techniques are employed to study the accuracy of the scalar-field analysis of a class of specialty fibers, to advance fiber-optical atom-guiding schemes and the development of sensor fibers, and to investigate rotation-induced spectral effects in partially coherent fields.

The thesis presents guidelines for accurate modal analysis of the low-order modes in hollow-core and annular-core optical fibers in terms of weakly guided, scalar fields. It turns out that the scalar-field description is especially inaccurate when the thickness of the core is on the order of a few optical wavelengths. This finding suggests that the self-imaging capability of annular-core fibers, which is deduced by considering the scalar fields of the fiber, can in fact be much weaker than previously thought [14–16]. A rigorous, full-vector investigation of the self-imaging effect included in this thesis supports this conclusion. Furthermore, the analysis indicates that it is altogether difficult to find a decent regime for general-purpose (annular) self-imaging with such fibers.

In this thesis, two methods for obtaining a spatially smooth atom-guiding field on the inner surface of a hollow-core fiber are analyzed by making use of the weak-guidance approach. The first method is based on the selective excitation of tubular fiber modes with angular-momentum-carrying beams. In the second method [52], the incident angle of a Gaussian beam is rapidly dithered in time yielding a smooth, time-averaged atom-guiding field. Besides fiber-optical atom guiding [49] and trapping [86], such smooth time-average fields have recently been applied, e.g., in the delivery of high-peak-power nanosecond pulses for fluid flow measurements [87].

In this thesis, the spectral transmission characteristics of photonic-bandgap and index-guiding fibers with coated inclusions are specified. Dielectric inclusions are considered with the bandgap fiber, whereas the index-guiding, microstructured fiber is assumed to additionally contain metal inclusions to permit the excitation of surface-plasmon-polariton resonances. Such resonances can be employed in the construction of compact, fiber-integrated (bio)sensor devices for which a novel design is proposed in this thesis. The design makes use of a three-hole microstructured fiber with uniform gold and low-refractive-index dielectric inclusions. Besides uniform metal layers, it is possible to fabricate micrometer-scale metal structures within the holes of a microstructured fiber [19]. In addition to miniaturized in-fiber devices, these structures are potentially useful in future fiber-integrated plasmonic applications [88].

The thesis also includes an investigation of the rotational frequency shifts in partially coherent fields. The field realizations are expanded in terms of angular-momentum-carrying modes which contribute to the overall spectral change due to the rotation. Such changes are not only of fundamental interest but can also be beneficial to remote-sensing and gyroscopic technologies [89]. The angular-momentum-carrying, vortical modes themselves have found numerous applications ranging from optical spanning to quantum entanglement [90, 91]. Recently, helical-core fibers allowing the propagation of a single helical mode have been introduced [92].

Besides performing modal analyses for given fiber profiles, one can also find the inverse process meaningful, i.e., the determination of a refractive-index profile which would yield a desired modal field. This would be especially useful in tailoring the output field of a fiber for applications, e.g., in particle trapping and guiding, materials processing, and lighting. Genetic algorithms can prove to be helpful in the design process [93].

Bibliography

[1] B. E. A. Saleh, and M. C. Teich, *Fundamentals of Photonics*, 2nd Ed. (John Wiley & Sons, Inc., Hoboken, New Jersey, 2007).

[2] P. Russell, "Photonic crystal fibers," Science **299,** 358–362 (2003).

[3] J. Toulouse, "Optical nonlinearities in fibers: review, recent examples, and systems applications," J. Lightw. Technol. **23,** 3625–3641 (2005).

[4] J. Wang, X. Yang, and L. Wang, "Fabrication and experimental observation of monolithic multi-air-core fiber array for image transmission," Opt. Express **16,** 7703–7708 (2008).

[5] F. T. S. Yu and S. S. Yin, eds., *Fiber Optic Sensors* (Marcel Dekker, Inc., New York, 2002).

[6] A. K. Sharma, R. Jha, and B. D. Gupta, "Fiber-optic sensors based on surface plasmon resonance: a comprehensive review," IEEE Sensors Journal **7,** 1118–1129 (2007).

[7] T. Ritari, J. Tuominen, H. Ludvigsen, J. Petersen, T. Sørensen, T. Hansen, and H. Simonsen, "Gas sensing using air-guiding photonic bandgap fibers," Opt. Express **12,** 4080–4087 (2004).

[8] F. Benabid, "Hollow-core photonic bandgap fibre: new light guidance for new science and technology," Phil. Trans. R. Soc. A **364,** 3439–3462 (2006).

[9] J. M. Dudley, G. Genty, and S. Coen, "Supercontinuum generation in photonic crystal fiber," Rev. Mod. Phys. **78,** 1135–1184 (2006).

[10] K. Oh, S. Choi, Y. Jung, and J. W. Lee, "Novel hollow optical fibers and their applications in photonic devices for optical communications," J. Lightw. Technol. **23,** 524–532 (2005).

[11] R. Taylor and C. Hnatovsky, "Particle trapping in 3-D using a single fiber probe with an annular light distribution," Opt. Express **11,** 2775–2782 (2003).

[12] D. Gloge, "Weakly guiding fibers," Appl. Opt. **10,** 2252–2258 (1971).

[13] H.-R. Noh and W. Jhe, "Atom optics with hollow optical systems," Phys. Rep. **372,** 269–317 (2002).

[14] C. Y. H. Tsao, D. N. Payne, and W. A. Gambling, "Modal characteristics of three-layered optical fiber waveguides: a modified approach," J. Opt. Soc. Am. A **6,** 555–563 (1989).

[15] N. B. Baranova and B. Ya. Zel'dovich, "Talbot effect for whispering gallery modes and modes of tubular waveguides," in technical digest of the International Quantum Electronics Conference, IQEC'98, San Francisco, California, US, May 3–4 1998, pp. 184–185.

[16] T. Niemeier and R. Ulrich, "Self-imaging by ring-core fibers," in *Digest of Topical Meeting on Optical Fiber Communication,* I. D. Aggarwal, ed., Washington D.C., US, 1985, pp. 122–124.

[17] M. Wrage, P. Glas, D. Fischer, M. Leitner, N. N. Elkin, D. V. Vysotsky, A. P. Napartovich, and V. N. Troshchieva, "Phase-locking of a multicore fiber laser by wave propagation through an annular waveguide," Opt. Commun. **205,** 367–375 (2002).

[18] A. P. Napartovich and D. V. Vysotsky, "Phase-locking of multicore fibre laser due to Talbot self-reproduction," J. Mod. Opt. **50,** 2715–2725 (2003).

[19] P. J. A. Sazio, A. Amezcua-Correa, C. E. Finlayson, J. R. Hayes, T. J. Scheidemantel, N. F. Baril, B. R. Jackson, D.-J. Won, F. Zhang, E. R. Margine, V. Gopalan, V. H. Crespi, and J. V. Badding, "Microstructured optical fibers as high-pressure microfluidic reactors," Science **311,** 1583–1586 (2006).

[20] L. Allen, S. M. Barnett, and M. J. Padgett, eds., *Optical Angular Momentum* (IOP Publishing, Bristol, United Kingdom, 2003).

[21] J. D. Jackson, *Classical Electrodynamics*, 3rd Ed. (John Wiley & Sons, Inc., Hoboken, New Jersey, 1999).

[22] G. P. Agrawal, *Nonlinear Fiber Optics*, 3rd Ed. (Academic Press, San Diego, California, 2001).

[23] D. Marcuse, *Light Transmission Optics*, 2nd Ed. (Van Nostrand Reinhold Company, New York, 1982).

[24] L. Novotny and B. Hecht, *Principles of Nano-Optics* (Cambridge University Press, Cambridge, UK, 2006).

[25] M. Born and E. Wolf, *Principles of Optics*, 7th Ed. (Cambridge University Press, Cambridge, UK, 1999).

[26] A. W. Snyder and J. D. Love, *Optical Waveguide Theory* (Chapman & Hall, London, 1983).

[27] M. Nieto-Vesperinas, *Scattering and Diffraction in Physical Optics* (John Wiley & Sons, Inc., New York, 1991).

[28] J. D. Joannopoulos, R. D. Meade, and J. N. Winn, *Photonic Crystals: Molding the Flow of Light* (Princeton University Press, Singapore, 1995).

[29] J. Broeng, S. E. Barkou, T. Søndergaard, and A. Bjarklev, "Analysis of air-guiding photonic bandgap fibers," Opt. Lett. **25,** 96–98 (2000).

[30] F. Brechet, J. Marcou, D. Pagnoux, and P. Roy, "Complete analysis of the characteristics of propagation into photonic crystal fibers, by the finite element method," Opt. Fiber Technol. **6,** 181–191 (2000).

[31] S. Selleri, L. Vincetti, A. Cucinotta, and M. Zoboli, "Complex FEM modal solver of optical waveguides with PML boundary conditions," Opt. Quant. Electr. **33,** 359–371 (2001).

[32] P. W. Milonni and R. D. Meade, and J. H. Eberly, *Lasers* (John wiley & Sons, Inc., New York, 1988).

[33] Y. Ohtake, T. Ando, N. Fukuchi, N. Matsumoto, H. Ito, and T. Hara, "Universal generation of higher-order multiringed Laguerre–Gaussian beams by using a spatial light modulator," Opt. Lett. **32,** 1411–1413 (2007).

[34] A. S. Desyatnikov, Yu. S. Kivshar, and L. Torner, "Optical vortices and vortex solitons," in *Progress in optics*, Vol. 47, E. Wolf, ed., (Elsevier, Amsterdam, 2005).

[35] M. W. Beijersbergen, L. Allen, H. E. L. O. van der Veen and J. P. Woerdman, "Astigmatic laser mode converters and transfer of orbital angular momentum," Opt. Commun. **96,** 123–132 (1993).

[36] W. M. Lee, X.-C. Yuan, and K. Dholakia, "Experimental observation of optical vortex evolution in a Gaussian beam with an embedded fractional phase step," Opt. Commun. **239,** 129–135 (2004).

[37] L. Allen, M. W. Beijersbergen, R. J. C. Spreeuw, and J. P. Woerdman, "Orbital angular momentum of light and the transformation of Laguerre-Gaussian laser modes," Phys. Rev. A **45,** 8185–8189 (1992).

[38] L. Allen and M. J. Padgett, "The Poynting vector in Laguerre–Gaussian beams and the interpretation of their angular momentum density," Opt. Commun. **184,** 67–71 (2000).

[39] J. Courtial, D. A. Robertson, K. Dholakia, L. Allen, and M. J. Padgett, "Rotational frequency shift of a light beam," Phys. Rev. Lett. **81,** 4828–4830 (1998).

[40] L. Mandel and E. Wolf, *Optical Coherence and Quantum Optics* (Cambridge University Press, Cambridge, UK, 1995).

[41] B. Zhang and B. Lü, "Transformation of Gaussian Schell-model beams and their coherent-mode representation," J. Optics (Paris) **27,** 99–103 (1996).

[42] O. Svelto, *Principles of Lasers,* 4th Ed. (Plenum Press, New York, 1998).

[43] G. Volpe and D. Petrov, "Generation of cylindrical vector beams with few-mode fibers excited by Laguerre–Gaussian beams," Opt. Commun. **237,** 89–95 (2004).

[44] P. R. Chaudhuri, C. Lu, and W. Xiaoyan, "Scalar model and exact vectorial description for the design analysis of hollow optical fiber components," Opt. Commun. **228,** 285–293 (2003).

[45] H. Ito, K. Sakaki, T. Nakata, W. Jhe, and M. Ohtsu, "Optical potential for atom guidance in a cylindrical-core hollow fiber," Opt. Commun. **115,** 57–64 (1995).

[46] M. J. Renn and R. Pastel, "Particle manipulation and surface patterning by laser guidance," J. Vac. Sci. Technol. B **16,** 3859–3863 (1998).

[47] M. J. Renn, D. Montgomery, O. Vdovin, D. Z. Anderson, C. E. Wieman, and E. A. Cornell, "Laser-guided atoms in hollow-core optical fibers," Phys. Rev. Lett. **75,** 3253–3256 (1995).

[48] M. J. Renn, A. A. Zozulya, E. A. Donley, E. A. Cornell, and D. Z. Anderson, "Optical-dipole-force fiber guiding and heating of atoms," Phys. Rev. A **55,** 3684–3696 (1996).

[49] F. Fatemi, M. Bashkansky, and S. Moore, "Side-illuminated hollow-core optical fiber for atom guiding," Opt. Express **13,** 4890–4895 (2005).

[50] M. J. Renn, E. A. Donley, E. A. Cornell, C. E. Wieman, and D. Z. Anderson, "Evanescent-wave guiding of atoms in hollow optical fibers," Phys. Rev. A **53,** R648-R651 (1996).

[51] Z. Bouchal, O. Haderka, and R. Celechovsky, "Selective excitation of vortex fibre modes using a spatial light modulator," New. J. Phys. **7,** 125 (2005).

[52] D. Müller, E. A. Cornell, D. Z. Anderson, and E. R. I. Abraham, "Guiding laser-cooled atoms in hollow-core fibers," Phys. Rev. A **61,** 033411 (2000).

[53] M. H. Anderson, J. R. Ensher, M. R. Matthews, C. E. Wieman, and E. A. Cornell, "Observation of Bose–Einstein condensation in a dilute atomic vapor," Science **296,** 198–201 (1995).

[54] N. Friedman, L. Khaykovich, R. Ozeri, and N. Davidson, "Compression of cold atoms to very high densities in a rotating-beam blue-detuned optical trap," Phys. Rev. A **61,** 031403(R) (2000).

[55] Crystal Fibre A/S; http://www.crystalfibre.com/

[56] T. M. Monro and H. Ebendorff-Heidepriem, "Progress in microstructured optical fibers," Annu. Rev. Mater. Res. **36,** 467–495 (2006).

[57] J. M. Fini, "Microstructure fibres for optical sensing in gases and liquids," Meas. Sci. Technol. **15,** 1120–1128 (2004).

[58] A. Hassani and M. Skorobogatiy, "Design of the microstructured optical fiber-based surface plasmon resonance sensor with enhanced microfluidics," Opt. Express **14,** 11616–11621 (2006).

[59] A. Hassani and M. Skorobogatiy, "Design criteria for microstructured-optical-fiber-based surface-plasmon-resonance sensors," J. Opt. Soc. Am. B **24,** 1423–1429 (2007).

[60] B. Gauvreau, A. Hassani, M. F. Fehri, A. Kabashin, and M. Skorobogatiy, "Photonic bandgap fiber-based surface plasmon resonance sensors," Opt. Express **15,** 11413–11426 (2007).

[61] A. Bjarklev, J. Broeng, and A. S. Bjarklev, *Photonic Crystal Fibres* (Kluwer Academic Publishers, Boston, 2003).

[62] N. A. Mortensen and M. D. Nielsen, "Modeling of realistic cladding structures for air-core photonic bandgap fibers," Opt. Lett. **29,** 349–351 (2004).

[63] S. G. Johnson and J. D. Joannopoulos, "Block-iterative frequency-domain methods for Maxwell's equations in a planewave basis," Opt. Express **8,** 173–190 (2001).

[64] The MIT Photonic-Bands (MPB) package; http://ab-initio.mit.edu/wiki/

[65] M. Hautakorpi, H. Hoffrén, J. Tiilikainen, and H. Ludvigsen, "Photonic bandgaps in photonic crystal fibers with coated high-index inclusions," in *Conference on Lasers and Electro-Optics (CLEO/QELS 07),* Baltimore, Maryland, US, May 6–11 2007, paper JTuA65.

[66] X. Zhang, R. Wang, F. Cox, B. T. Kuhlmey, and M. C. J. Large, "Selective coating of holes in microstructured optical fiber and its application to in-fiber absorptive polarizers," Opt. Express **15,** 16270–16278 (2006).

[67] A. Amezcua-Correa, J. Yang, C. E. Finlayson, A. C. Peacock, J. R. Hayes, P. J. A. Sazio, J. J. Baumberg, and S. M. Howdle, "Surface-enhanced Raman scattering using microstructured optical fiber substrates," Adv. Funct. Mater. **17,** 2024–2030 (2007).

[68] A. V. Zayats, I. I. Smolyaninov, and A. A. Maradudin, "Nano-optics of surface plasmon polaritons," Phys. Rep. **408,** 131–314 (2005).

[69] W. L. Barnes, A. Dereux, and T. W. Ebbesen, "Surface plasmon subwavelength optics," Nature **424,** 824–830 (2003).

[70] E. Ozbay, "Plasmonics: merging photonics and electronics at nanoscale dimensions," Science **311,** 189–193 (2006).

[71] A. Campion and P. Kambhampati, "Surface-enhanced Raman scattering," Chem. Soc. Rev. **27,** 241–250 (1998).

[72] M. D. Porter, R. J. Lipert, L. M. Siperko, G. Wangb and R. Narayanana, "SERS as a bioassay platform: fundamentals, design, and applications," Chem. Soc. Rev. **37,** 1001–1011 (2008).

[73] J. Homola, "Present and future of surface plasmon resonance biosensors," Anal. Bioanal. Chem **377,** 528–539 (2003).

[74] J. Homola, S. S. Yee, and G. Gauglitz, "Surface plasmon resonance sensors: review," Sensors and Actuators B **54,** 3–15 (1999).

[75] Fiber fabricated at the University of Marie Curie-Sklodowska, Lublin, Poland.

[76] C. M. B. Cordeiro, M. A. R. Franco, C. J. S. Matos, F. Sircilli, V. A. Serrão, and C. H. Brito Cruz, "Single-design-parameter microstructured optical fiber for chromatic dispersion tailoring and evanescent field enhancement," Opt. Lett. **32,** 3324–3326 (2007).

[77] COMSOL Multiphysics; http://www.comsol.com/

[78] E. Santamato, "Photon orbital angular momentum: problems and perspectives," Fortschr. Phys. **52,** 1141–1153 (2004).

[79] N. B. Simpson, K. Dholakia, L. Allen, and M. J. Padgett, "Mechanical equivalence of spin and orbital angular momentum of light: an optical spanner," Opt. Lett. **22,** 52–54 (1997).

[80] K. C. Neuman and S. M. Blocka, "Optical trapping," Rev. Sci. Instrum. **75,** 2787–2809 (2004).

[81] M. V. Vasnetsov, J. P. Torres, D. V. Petrov, and L. Torner, "Observation of the orbital angular momentum spectrum of a light beam," Opt. Lett. **28,** 2285–2287 (2003).

[82] R. Dasgupta and P. K. Gupta, "Measurement of orbital angular momentum of a single photon: a non-interferrometric approach," in *Proceedings of the 7th International Conference on Optoelectronics, Fiber Optics and Photonics,* Cochin, Kerala, India, 2004.

[83] J. Arlt, M. P. MacDonald, L. Paterson, W. Sibbett, K. Dholakia, and K. Volke-Sepulveda, "Moving interference patterns created using the angular Doppler effect," Opt. Express **10,** 844–852 (2002).

[84] M. Babiker and S. Al-Awfi, "Light-induced rotational effects in atom guides," Opt. Commun. **168,** 145–150 (1999).

[85] I. Bialynicki-Birula and Z. Bialynicka-Birula, "Rotational frequency shift," Phys. Rev. Lett. **78,** 2539–2542 (1997).

[86] A. P. Povilus, S. E. Olson, R. R. Mhaskar, B.-K. Teo, J. R. Guest, and G. Raithel, "Time averaging of multimode optical fiber output for a magneto-optical trap," J. Opt. Soc. Am. B **22,** 311–314 (2005).

[87] J. P. Parry, J. D. Shephard, J. D. C. Jones, and D. P. Hand, "Speckle contrast reduction in a large-core fiber delivering Q-switched pulses for fluid flow measurements," Appl. Opt. **45,** 4209–4218 (2006).

[88] J. Hou, D. Bird, A. George, S. Maier, B. T. Kuhlmey, and J. C. Knight, "Metallic mode confinement in microstructured fibres," Opt. Express **16,** 5983–5990 (2008).

[89] G. S. Agarwal and G. Gbur, "Rotational frequency shifts for electromagnetic fields of arbitrary states of coherence and polarization," Opt. Lett. **31,** 3080–3082 (2006).

[90] S. Franke-Arnold, L. Allen, and M. Padgett, "Advances in optical angular momentum," Laser & Photon. Rev. **2,** 299–313 (2008).

[91] G. Molina-Terriza, J. P. Torres, and L. Torner, "Twisted photons," Nature Physics **3,** 305–310 (2007).

[92] C. N. Alexeyev, B. P. Lapin, and M. A. Yavorsky, "Helical core optical fibers maintaining propagation of a solitary optical vortex," Phys. Rev. A **78,** 013813 (2008).

[93] R. R. Musin and A. M. Zheltikov, "Designing dispersion-compensating photonic-crystal fibers using a genetic algorithm," Opt. Commun. **281,** 567–572 (2008).

Abstracts of publications I–V

I. We study the applicability of the weakly guiding approximation (WGA) to the modal analysis of an M-type optical fiber in which a ring-shaped core lies between two uniform cladding layers. Besides being dependent on the refractive indices, the accuracy of the approximation is shown to be substantially affected by the transverse dimensions of the core. The accuracy is characterized by calculating an overlap integral between the exact and WGA-approximated modal fields. Fibers that have an inner cladding similar to the outer cladding, or similar to vacuum, are considered in detail. The feasibility of the WGA in determining the fiber parameters for single-mode guidance is also discussed.

II. We analyze two methods for obtaining a smooth evanescent-wave intensity profile on the inner surface of a multimode hollow optical fiber to be used as a waveguide for neutral atoms. The first method is based on the selective excitation of fiber modes with a laser beam possessing orbital angular momentum, of which Laguerre–Gaussian beams are considered as an example. The second method makes use of a rapid variation of the speckle pattern of the fiber's evanescent-wave in the timescale of the atomic motion. The variation is provided by dithering the angle of incidence of a Gaussian laser beam at the fiber entrance. The optimal beam waist and direction of dithering are determined.

III. We investigate the occurrence of self-images, or Talbot images, in a spatially multimode field that propagates along an optical fiber whose core has an annular-shaped cross section. By use of full-vectorial modal analysis, we study the effect of the transverse fiber dimensions on the self-imaging properties. According to our analysis, good self-images can be expected when the fiber core is thin and the modes are far from their cutoffs. However, as the core diameter is made larger to increase the number of modes available in the imaging, the general self-imaging properties tend to deteriorate.

IV. We propose a novel surface-plasmon-resonance sensor design based on coating the holes of a three-hole microstructured optical fiber with a low-index dielectric layer on top of which a gold layer is deposited. The use of all three fiber holes and their relatively large size should facilitate the fabrication of the inclusions and the infiltration of the analyte. Our numerical results indicate that the optical loss of the Gaussian guided mode can be made very small by tuning the thickness of the dielectric layer and that the refractive-index resolution for aqueous analytes is 1×10^{-4}.

V. We study the frequency shifts taking place when a random, stationary optical field rotates with respect to an observer. The field is expanded in terms

of fully coherent Laguerre–Gaussian basis modes, for which the rotational frequency shifts have been studied previously. We demonstrate the formalism by considering the spectrum of a Gaussian Schell-model field, and show that for a spatially highly incoherent field, significant spectral changes can be expected.

ISBN 978-951-22-9631-6
ISBN 978-951-22-9632-3 (PDF)
ISSN 1795-2239
ISSN 1795-4584 (PDF)